

UNCLASSIFIED

AD NUMBER

ADB002919

LIMITATION CHANGES

TO:

Approved for public release; distribution is unlimited.

FROM:

Distribution authorized to U.S. Gov't. agencies only; Test and Evaluation; SEP 1974. Other requests shall be referred to Air Force Avionics Laboratory, Wright-Patterson AFB OH 45433.

AUTHORITY

AFAL per DTIC form 55

THIS PAGE IS UNCLASSIFIED

THIS REPORT HAS BEEN DELIMITED
AND CLEARED FOR PUBLIC RELEASE
UNDER DOD DIRECTIVE 5200.20 AND
NO RESTRICTIONS ARE IMPOSED UPON
ITS USE AND DISCLOSURE.

DISTRIBUTION STATEMENT A

APPROVED FOR PUBLIC RELEASE;
DISTRIBUTION UNLIMITED.

AD B002919

MAGNETIC BUBBLE RESEARCH

F. G. West
D. C. Bullock
J. T. Carlo
W. C. Hubbell
J. C. Linn
R. A. Naden
C. T. M. Chang

Texas Instruments Incorporated

September 1974

Third Interim Report for Period 16 November 1973 - 15 May 1974



Distribution limited to U. S. Government agencies only; test and evaluation results reported: September 1974. Other requests for this document must be referred to AFAL/TEA, Wright-Patterson AFB, Ohio 45433.

Air Force Avionics Laboratory
Wright-Patterson Air Force Base, Ohio

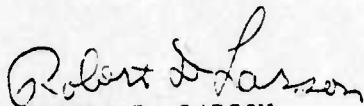


NOTICE

When Government drawings, specifications, or other data are used for any purpose other than in connection with a definitely related Government procurement operation, the United States Government thereby incurs no responsibility nor any obligation whatsoever; and the fact that the government may have formulated, furnished, or in any way supplied the said drawings, specifications, or other data, is not to be regarded by implication or otherwise as in any manner licensing the holder or any other person or corporation, or conveying any rights or permission to manufacture, use, or sell any patented invention that may in any way be related thereto.

This report has been reviewed and is approved for publication.

FOR THE COMMANDER



ROBERT D. LARSON
Chief, Advanced Electronic Devices Branch
Electronic Technology Division
Air Force Avionics Laboratory

Copies of this report should not be returned unless return is required by security considerations, contractual obligations, or notice on a specific document.

UNCLASSIFIED

SECURITY CLASSIFICATION OF THIS PAGE (When Data Entered)

REPORT DOCUMENTATION PAGE		READ INSTRUCTIONS BEFORE COMPLETING FORM
1. REPORT NUMBER AFAL-TR-74-196	2. GOVT ACCESSION NO.	3. RECIPIENT'S CATALOG NUMBER
4. TITLE (and Subtitle) Magnetic Bubble Research		5. TYPE OF REPORT & PERIOD COVERED Interim Technical Report No.3 16 Nov. 1973 - 15 May 1974
		6. PERFORMING ORG. REPORT NUMBER 08-74-41
7. AUTHOR(s) F. G. West W. C. Hubbell C. T. M. Chang D. C. Bullock J. C. Linn J. T. Carlo R. A. Naden		8. CONTRACT OR GRANT NUMBER(s) F33615-73-C-1029
9. PERFORMING ORGANIZATION NAME AND ADDRESS Texas Instruments Incorporated Central Research Laboratories P. O. Box 5936, Dallas, Texas 75222		10. PROGRAM ELEMENT, PROJECT, TASK AREA & WORK UNIT NUMBERS
11. CONTROLLING OFFICE NAME AND ADDRESS Air Force Avionics Laboratory Wright-Patterson AFB, Ohio		12. REPORT DATE September 1974
		13. NUMBER OF PAGES 65
14. MONITORING AGENCY NAME & ADDRESS (if different from Controlling Office)		15. SECURITY CLASS. (of this report) UNCLASSIFIED
		15a. DECLASSIFICATION/DOWNGRADING SCHEDULE
16. DISTRIBUTION STATEMENT (of this Report) Distribution limited to U. S. Government agencies only; test and evaluation results reported: September 1974. Other requests for this document must be referred to AFAL/TEA, Wright-Patterson AFB, Ohio 45433.		
17. DISTRIBUTION STATEMENT (of the abstract entered in Block 20, if different from Report)		
18. SUPPLEMENTARY NOTES		
19. KEY WORDS (Continue on reverse side if necessary and identify by block number)		
20. ABSTRACT (Continue on reverse side if necessary and identify by block number) Section I of this report treats progress toward a complete conceptual design for the all-bubble processor described in AFAL-TR-74-19. Logic requirements for control and arithmetic functions are discussed in detail. One of the arithmetic units, a Full-Adder, was configured using three different, but complete, sets of logic elements. The result of this exercise is the specifi- cation of the complexity of the designs in terms of number of individual logic elements required.		

DD FORM 1 JAN 73 147

EDITION OF 1 NOV 65 IS OBSOLETE

UNCLASSIFIED

SECURITY CLASSIFICATION OF THIS PAGE (When Data Entered)

UNCLASSIFIED

SECURITY CLASSIFICATION OF THIS PAGE(When Data Entered)

Section II treats the continuing work on hybrid technologies. Experimental results relevant to the use of integrated optics for bubble detection are presented.

Experience with a Permalloy AND/OR gate is reported in Section III, and some of the difficulties expected in realizing Permalloy logic are pointed out. Results for e-beam patterned and plated Permalloy processed circuits having approximately $0.4\text{ }\mu\text{m}$ linewidth geometries are given, and it is concluded that both processing and garnet material capability should now allow successful device fabrication. Lastly, progress toward identifying and remedying problems associated with ion-implant propagation structures is reported.

UNCLASSIFIED

SECURITY CLASSIFICATION OF THIS PAGE(When Data Entered)

FOREWORD

This report was prepared by Texas Instruments Incorporated, Dallas, Texas, under Air Force Contract No. F33615-73-C-1029. The work under this contract is administered by the Air Force Avionics Laboratory, Wright-Patterson Air Force Base, Ohio. Mrs. E. A. Buvinger, AFAL/TEA, is Contract Monitor.

At Texas Instruments the work is being performed principally in the Physical Sciences Research Laboratory, part of TI's Central Research Laboratories. F. G. West is Program Manager, and Dr. D. C. Bullock is Principal Investigator.

This is the third Interim Technical Report for Contract No. F33615-73-C-1029. It covers the interim period of the contract from 16 November 1973 through 15 May 1974. It was submitted by the authors in May 1974. The first Interim Technical Report for Contract No. F33615-73-C-1029 (AFAL-TR-73-306) covered the period from 16 October 1972 through 30 April 1973. The second Interim Technical Report (AFAL-TR-74-19) covered the period from 30 April 1973 through 15 November 1973.

Texas Instruments report number is 08-74-41.

TABLE OF CONTENTS

<u>Section</u>		<u>Page</u>
I	PROGRESS ON TASK I, CONCEPTUALIZATION OF DATA PROCESSING FUNCTIONS	1
	A. Progress on An All-Bubble, One-Chip, Processor	1
	B. Status of One-Chip Bubble Processor Design . . .	25
II	PROGRESS ON TASK II, CONCEPTUALIZATION OF HYBRID TECHNOLOGIES	29
	A. Optical Waveguide Structures	29
	1. Summary	29
	2. Experimental Results on Magneto optic Modulation of Light Propagating by Internal Reflection	29
	3. Experimental Results on Waveguiding Confined to the Garnet Film	34
	4. Experimental Results on Ion Implanted Waveguides	38
	B. Bubble/Elastic Wave Interactions	
	1. Experimental Observation of Stripe Domain Interaction with Bulk Elastic Waves	42
	2. Surface Wave Interactions	43
III	PROGRESS ON TASK III, EXPERIMENTATION TO ESTABLISH PERFORMANCE OF INDIVIDUAL DEVICE ELEMENTS	45
	A. Logic Hardware	45
	1. Bubble Switch	45
	2. The AND/OR Gate	45
	3. Other Logic Elements	48
	B. Small Geometry Permalloy Circuits for Sub- micrometer Diameter Bubbles	49
	1. E-beam Patterning and Device Processing . .	49
	2. Garnet Material for Small Bubbles	57
	C. Ion-Implant Field Access Circuits	60

LIST OF TABLES

<u>Table</u>		<u>Page</u>
I	Truth Table for Control of Multifunction ALU	3
II	Three Candidate Sets of Logic Elements	23
III	Device Element Count for Full-Adder Circuits	24
IV	Synchronous Angles for TE Modes	36
V	Permalloy Film Plating Results	51

LIST OF ILLUSTRATIONS

<u>Figure</u>		<u>Page</u>
1	Multifunction Serial ALU	2
2	Resident and Transient Bubble Switches	4
3	Memory Access Synchronizers	6
4(a)	Resident Bubble Switch	8
4(b)	A "T" Flip-Flop Using a Resident Bubble Switch . . .	8
5	Synchronous "Resident Bubble" Switch	10
6	One-of-Sixteen Encoded Address Data Router	11
7	One-of-Sixteen Encoded Address Data Router Using Resident Bubble Switches	12
8	Memory Access Delay Network (Coarse) Using Only Transient Bubble Logic	14
9	Memory Access Delay Network (Fine) Using Only Transient Bubble Logic	15
10	Memory Access Delay Network (Coarse) Using Resident Bubble Logic	17
11	Memory Access Delay Network (Fine) Using Resident Bubble Logic	18
12	Full Adder Using Logic Set I Elements	19

LIST OF ILLUSTRATIONS
(continued)

<u>Figure</u>		<u>Page</u>
13	Full Adder Using Logic Set II Elements	20
14	Full Adder Using Logic Set III Elements	21
15	Demultiplexer Circuit	26
16	Storage Register	27
17	Fast Multiplier Circuit	28
18	Geometry for Internal Reflection Inside the Composite Bubble Film/Substrate	30
19	Experimental Optical Modulation Apparatus Using an Internally Reflected Beam	32
20	Percent Modulation Versus Magnetic Field Amplitude	33
21	Experimental Arrangement for Observation of m-Lines	37
22(a)	Implanted Film Geometry	39
22(b)	Unimplanted Film Geometry	39
23(a)	Bubble Switch	46
23(b)	AND/OR Gate	46
24	Permalloy AND/OR Gate	47
25	Permalloy Crossover Circuit	50
26	Optical Micrographs of E-Beam Patterned T-Bar Fields	53
27	Scanning Electron Micrographs of 750 Å Thick Permalloy Elements	54
28	Scanning Electron Micrographs of 1700 Å Thick Permalloy Elements	55
29	Scanning Electron Micrographs of 3800 Å Thick Permalloy Elements	56
30	Effect of an In-Plane Uniaxial Component of Anisotropy	62

SECTION I
PROGRESS ON TASK I,
CONCEPTUALIZATION OF DATA PROCESSING FUNCTIONS

A. Progress on An All-Bubble, One-Chip, Processor

Status Report No. 14 (December 1973) describes the design of an arithmetic-logic unit (ALU) for the one-chip bubble processor and describes the resident bubble switch logic element.

The ALU design is given in Figure 1. This unit has the capability of providing eight logical functions of the two input variables A and B, as listed in Table I. The design is based on the use of resident-bubble switches as described in References 1 and 2. These switches are similar to the transient switches described in AFAL TR-74-19, except that the control bubble "C" remains in place indefinitely until a second control bubble is sent to dislodge it. The symbols for transient and resident switches are shown in Figure 2. Permalloy pattern designs for both types of switches have been reported.¹ However, the actual construction will probably be more complicated than the rectangular geometries reported in Reference 1.

The design given in Figure 1 requires 5 resident-bubble switches, 7 transient switches, 11 bubble eaters, 14 exclusive merges, and 4 crossovers. Some of the elements used are required in several variations with respect to input and output orientations.

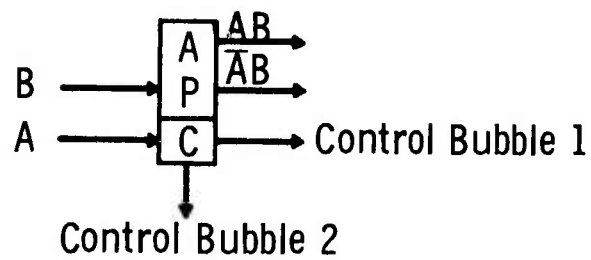
The ALU design given here can be used as part of an accumulator register in the one-chip bubble processor by linking the output $F(A,B)$ with the input B.

Table I
Truth Table for Control of Multifunction ALU
(0 - no resident bubble, 1 = resident bubble, x = don't care)

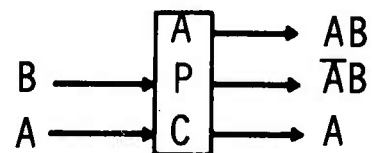
<u>C₁</u>	<u>C₂</u>	<u>C₃</u>	<u>C₄</u>	<u>C₅</u>	<u>F(A,B)</u>
1	x	1	0	0	A + B
0	1	1	0	0	A ⊕ B
0	0	1	0	0	AB
0	0	0	1	0	A plus B with carry
1	x	1	0	1	$\bar{A} + B$
0	1	1	0	1	$\bar{A} \oplus B$
0	0	1	0	1	$\bar{A}B$
0	0	0	1	1	A plus B with carry

The link would be a standard T-bar shift register with a capacity of 4N, where N is the word length. This is necessary because the carry loop in the full adder portion of the ALU requires that bubble pairs be input every fourth field cycle. The three voids between each bubble will also allow better margins for the logic gates by reducing unwanted data-dependent logic interactions. Further, the four-bubble spacing is consistent with the transfer spacing of bubbles coming to and from the all-bubble memory described in AFAL-TR-74-19.

Status Report No. 15 (January 1973) describes some of the control and timing elements proposed for the one-chip bubble processor. Included are: (1) a method for synchronizing the memory access with the control logic, (2) use of resident bubble switches to minimize control timing restrictions, (3) a design of a fully encoded address data router, and (4) a design for a memory access delay timer.



RESIDENT BUBBLE SWITCH



TRANSIENT BUBBLE SWITCH

Figure 2 Resident and Transient Bubble Switches

Two designs were completed for both the data router and the memory access timer, both with and without using resident bubble switches. The designs are compared to allow direct evaluation of the usefulness of the resident bubble switch as a logic element.

The control and timing function heavily taxes the resources of a mostly bubble processor. To provide the correct interaction of all the data, the instructions, and the control bubbles propagating on the numerous bubble propagation lines, the flow of data, instructions, and control must be precisely phased with one another. This leads to synchronous timing and control of the processing elements. Synchronous operation requires that transfer of data from memory, an inherently asynchronous process because of the arbitrary timing necessary to access a random memory address, must be synchronized with the other processing elements.

One method of synchronizing memory input and output is to use synchronizer/desynchronizer loops, as shown in Figure 3. The synchronizer loop holds an output word from the memory until it can be transferred in phase with the processor. Similarly, the desynchronizer loop holds an input word to the memory until the memory rotates into the correct position to accept it.

We have assumed that data propagates along propagation paths in the processor with the least significant bit leading. To ensure that the first bit transferred from the synchronizer is the least significant bit, this bit must appear at the synchronizer output gate on the arrival of the control bubble. This means that the loop must be fully populated when the control bubble arrives. Therefore, in this scheme the loop length must be an integer equal to the word length and have no common divisors with the integer spacing between bubbles arriving

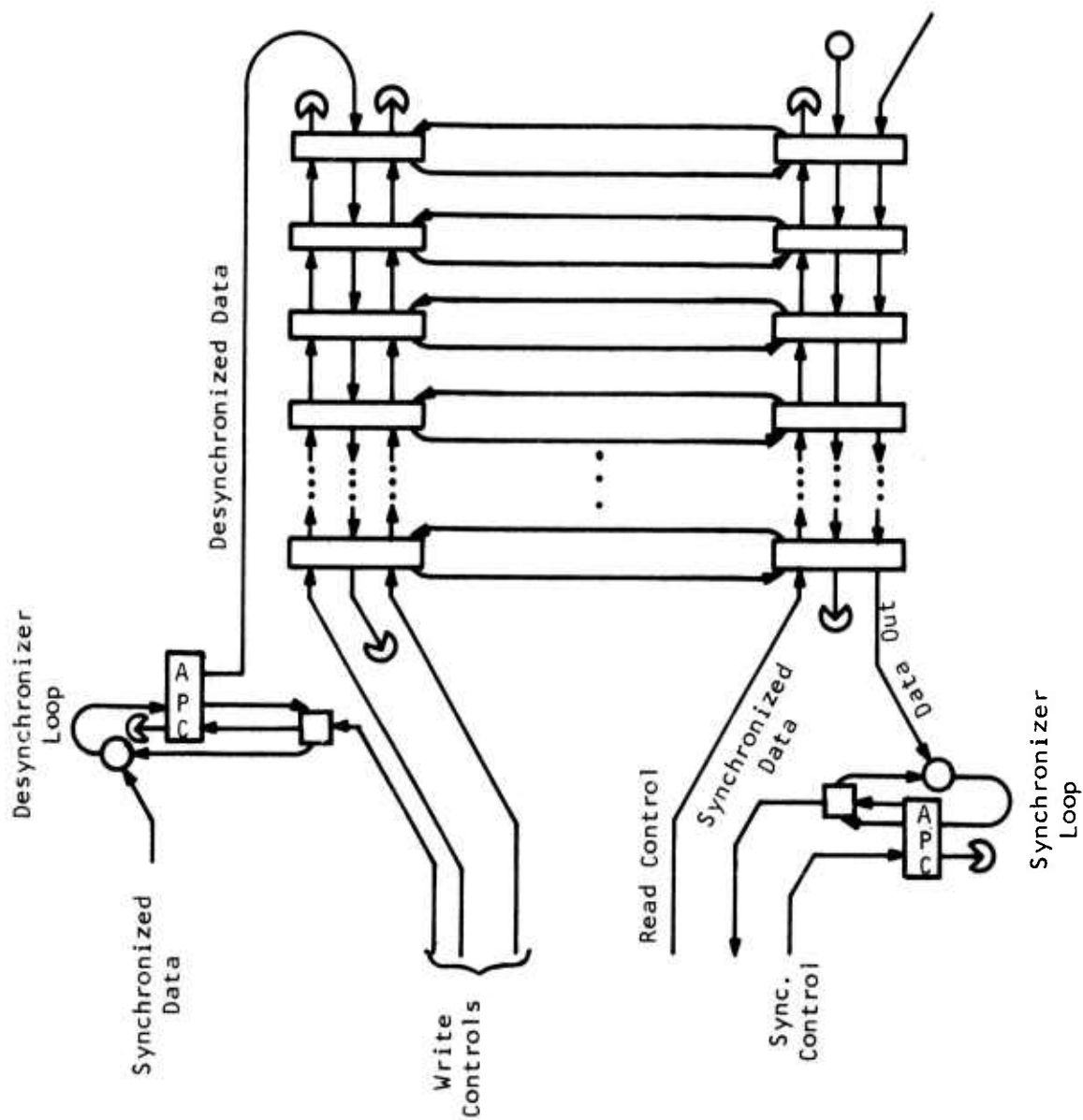


Figure 3 Memory Access Synchronizers

from the memory. This guarantees that the loop is fully populated. In addition, the bits from the memory must arrive at the synchronizer loop in a cyclically permuted order to ensure that the least significant bit is transferred first. This permutation is dependent on the memory address. For example, a word $a_0 a_1, \dots, a_{N-1}$ might be stored in location L as $a_i, a_{i+1}, \dots, a_{N-1}, a_0, \dots, a_{i-1}$, while it would be stored in location $L+1$ as $a_{i+1}, a_{i+2}, \dots, a_{N-1}, a_0, \dots, a_i$. Since the memory input desynchronizer will always perform the inverse permutation when loading a word into a location of memory, the scrambling of data in memory will be transparent to the rest of the processor.

The resident bubble switch has been described by Caron.³ This logic element seems to be valuable for magnetic bubble logic. Although all logic functions can be performed by using the transient bubble switch, crossover, exclusive merge, generator, annihilator, and propagation lines, the resident bubble switch allows a relaxation of many of the precise timing requirements necessary to perform logic functions.

A resident bubble switch is shown in Figure 4(a). The operation is very similar to that of the transient bubble switch described in AFAL-TR-74-19, except that the control bubble (RC) remains resident in the switch until it is pushed out by the input of another control bubble. When a control bubble is resident in the switch and another bubble arrives via input path C, both bubbles are expelled, one on each of the output paths from the resident control cell, leaving the RC location empty.

A resident bubble switch can be used as a flip-flop. An example of an RST flip-flop is shown in Figure 4(b).

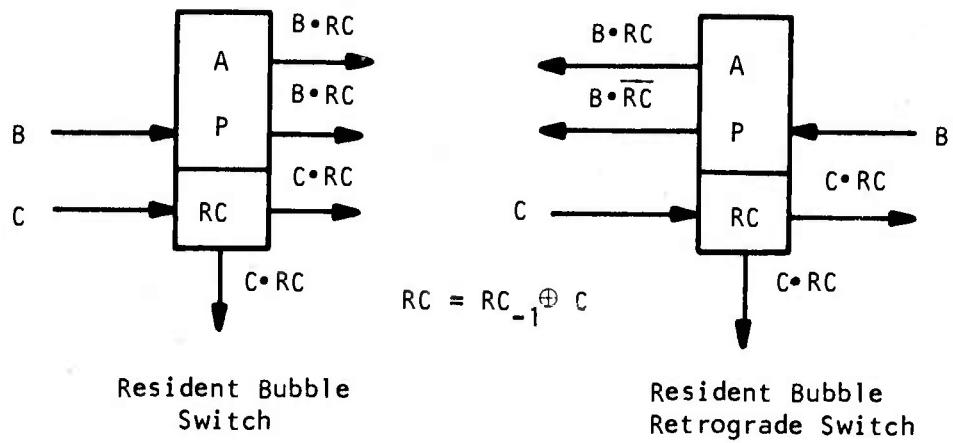


Figure 4(a) Resident Bubble Switch

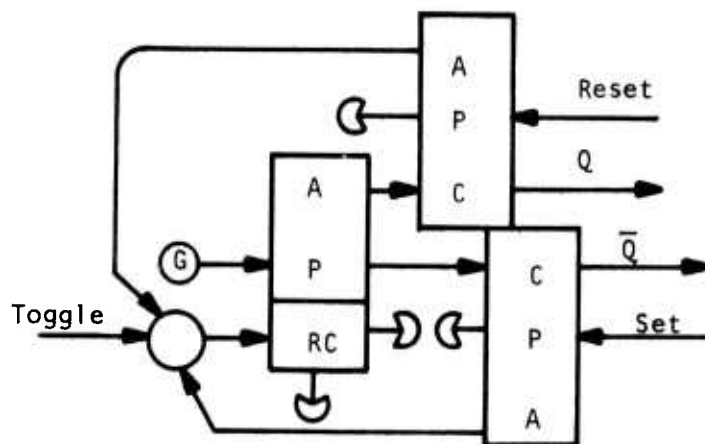


Figure 4(b) A "T" Flip-Flop Using a Resident Bubble Switch

To evaluate the usefulness of the resident bubble switch as a logic element, the designs of the data router and the memory access delay times were performed both with and without resident bubble switches. Use of the resident bubble switch relaxed the control, timing, and complexity requirements of asynchronous logic, while it had a very small effect on synchronous circuits. This is true because in synchronous logic, the operation of the resident bubble switch can be duplicated with a transient bubble switch with a small propagation loop on the control path, as shown in Figure 5. Here, the input B and the "set" and "clear" bubbles must come at specific times for the resident bubble to interact with the input.

Figure 6 shows the design of an encoded address data router (demultiplexer tree). An input bubble on path I is directed to path $P_{a_0 a_1 a_2 a_3}$ by inputting appropriately timed address bubbles on paths a_0 , a_1 , a_2 , and a_3 , respectively. An entire word can be routed through the network by inputting multiple address bubbles synchronously with the input bubbles, one set of address bubbles for each input bubble.

To enable one address bubble to control all the paths along one level of the tree, the address bubble must arrive at each switch exactly at the time that the data bubble arrives at the switch. This means that the path lengths of the tree must be carefully chosen. For example, path A in Figure 4 must be identical to the length of path B plus path C.

Figure 7 is a functionally equivalent design using resident bubble switches. Since each switch must have a resident bubble, the address bubbles must be duplicated for each switch. The address is input on lines a_0 , a_1 , a_2 , a_3 before the data arrives. All data input goes onto path $P_{a_0 a_1 a_2 a_3}$ until the address is reset. To reset the address, the old address is input again, forcing out the old bubbles, and the new address is sent along lines $a_0 a_1 a_2 a_3$.

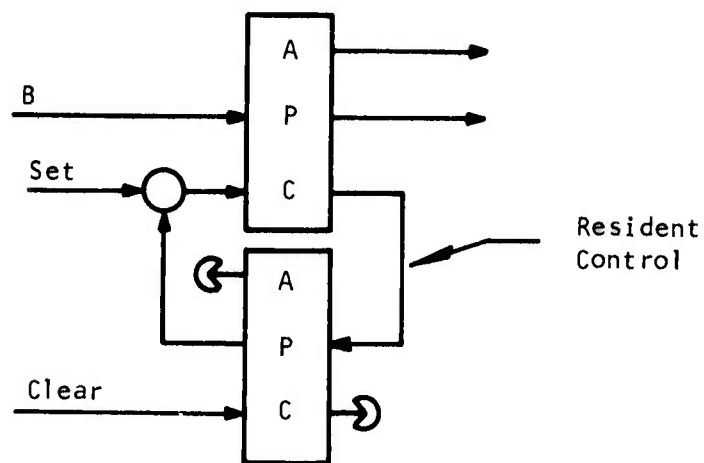


Figure 5 Synchronous "Resident Bubble" Switch

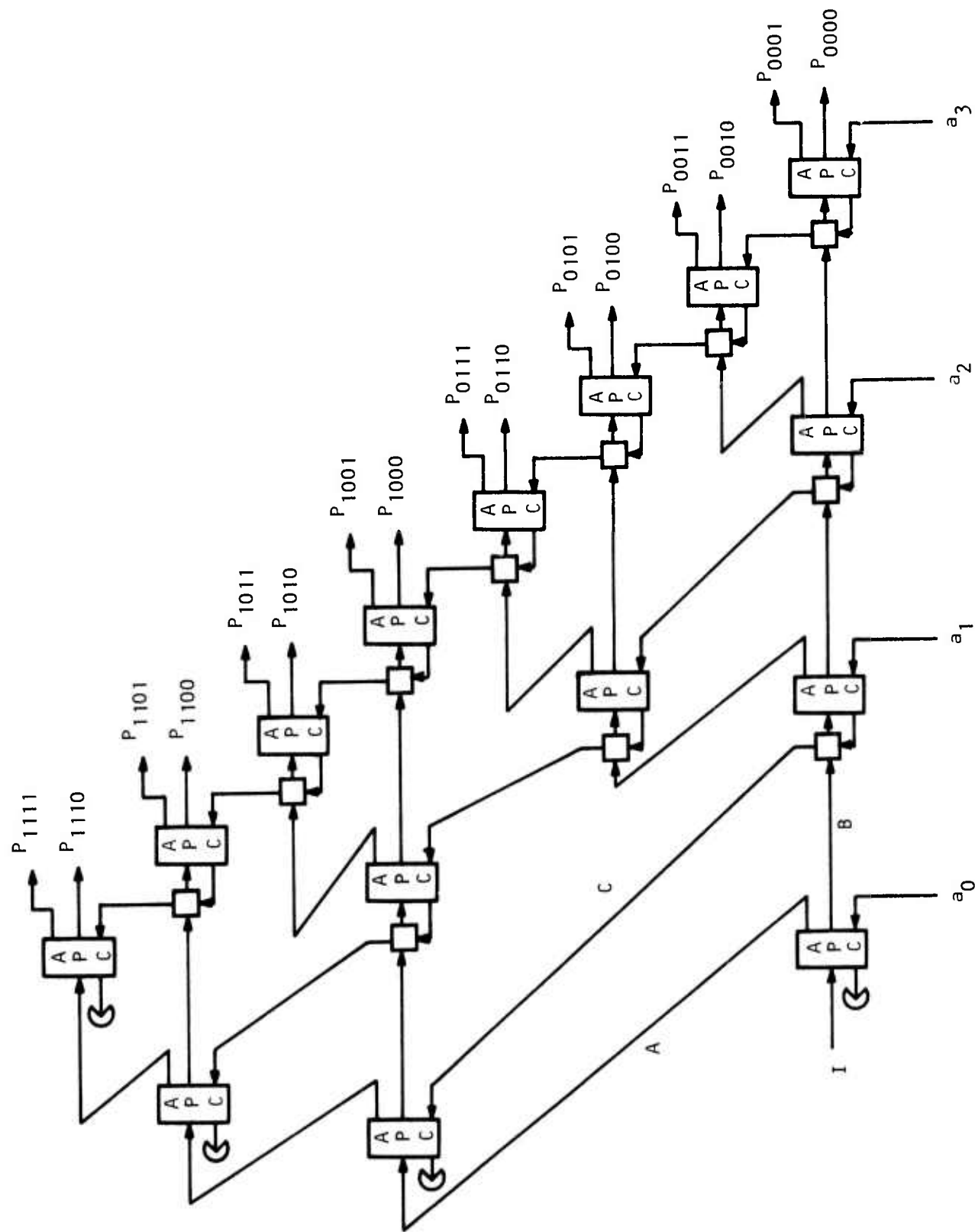


Figure 6 One-of-Sixteen Encoded Address Data Router

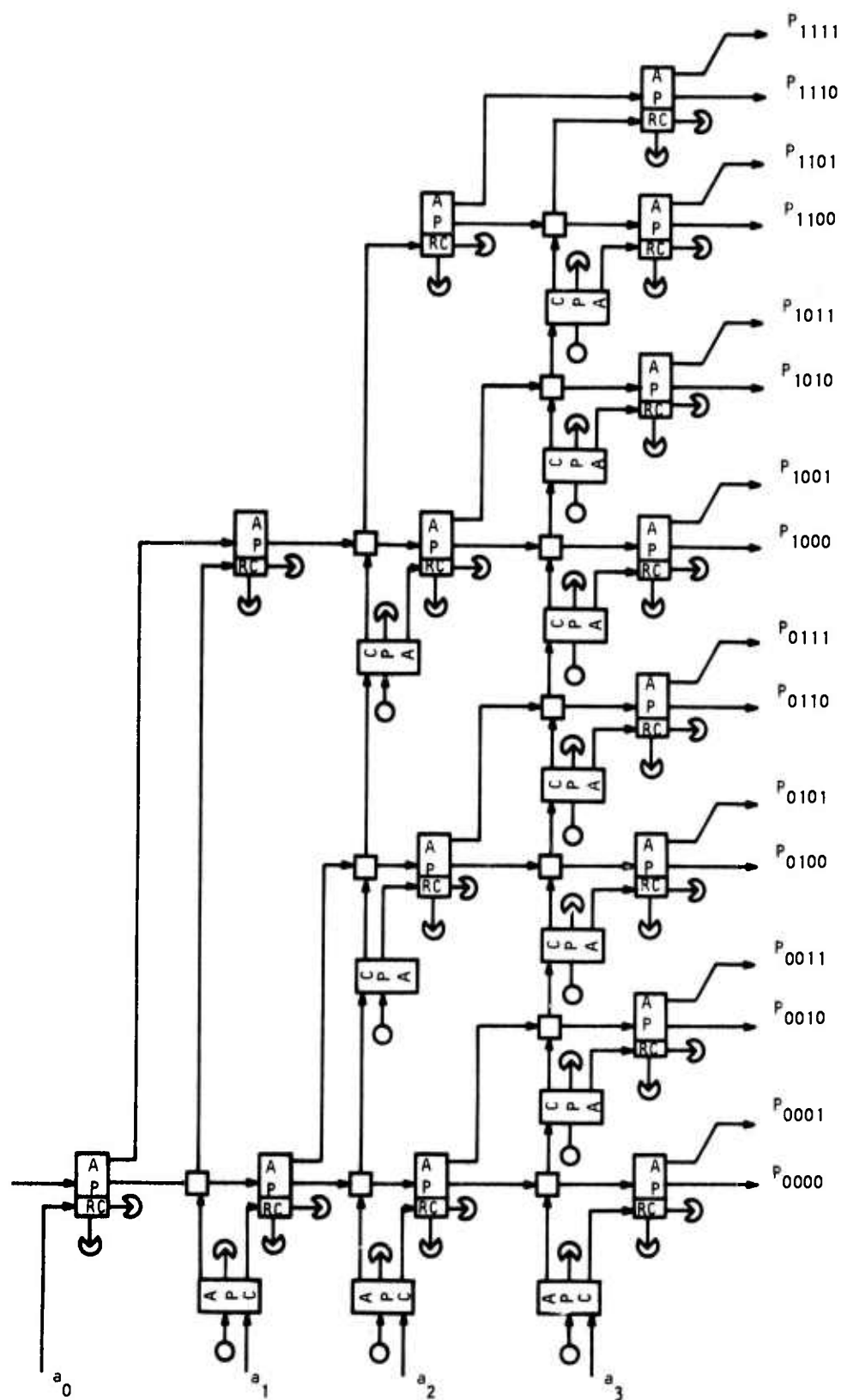


Figure 7 One-of-Sixteen Encoded Address Data Router Using Resident Bubble Switches

The all-bubble memory, previously described in AFAL-TR-74-19, is essentially asynchronous. To access an address in the memory, a bubble is sent down the read or write control lines at a specific time relative to the then rotational position of the address in the memory. This is independent of the phasing of the rest of the processor. One method of synchronizing the memory with the processor is to gate the memory address into a memory access delay timer at a specific moment in the rotation of the memory. The delay timer then produces an output bubble with a delay proportional to the value of the input address.

Figures 8 and 9 show a design for producing a bubble with delay determined by the value of the address. The network consists of two parts: a binary counter that determines a coarse delay proportional to the most significant bits of the address (Figure 8) and a fine delay caused by propagating the bubble along a variable path length determined by the least significant bits of the address (Figure 9). The binary counter is synchronous, while the fine delay circuit is essentially asynchronous. A binary counter alone cannot be used to create the time delay, since a binary counter for word length N made from bubble logic requires on the order of $4N$ to $5N$ magnetic field rotations to perform one increment of the counter. The fine delay, however, must be variable to within plus or minus one field rotation. The fine resolution in the delay must come from a variable path length.

In Figure 9 a data router is used to select the path of appropriate length to achieve the fine address resolution. The length of each consecutive path in the data router differs by one from the previous path. The least significant bits of the address, which determine the fine address, are entered into the loops L_1 , L_2 , L_3 , and L_4 until the output of the binary counter gates them into the data router.

Extract Low Order Bits (LOB)

Address (High Order Bits)

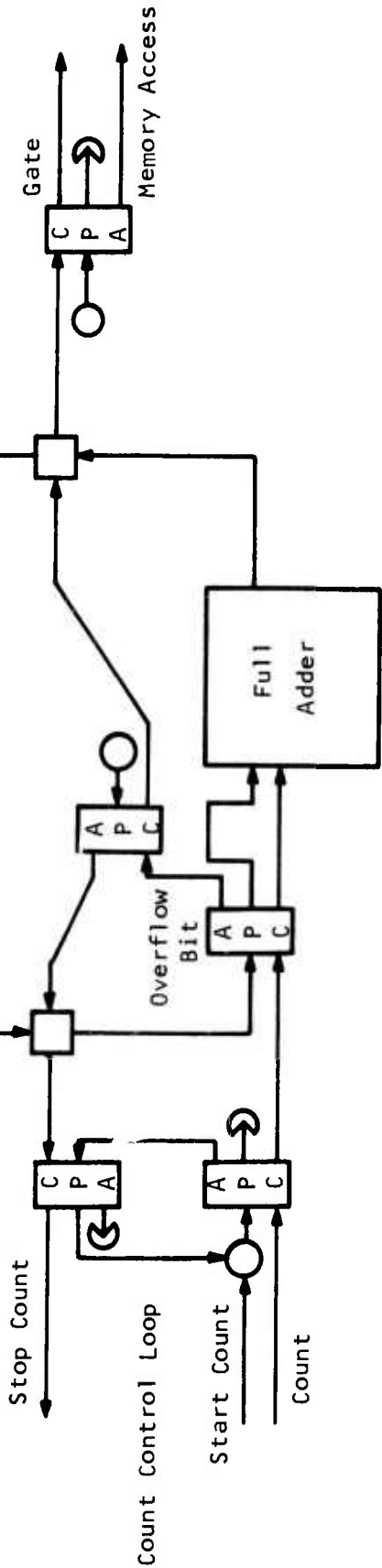


Figure 8 Memory Access Delay Network (Coarse) Using Only Transient Bubble Logic

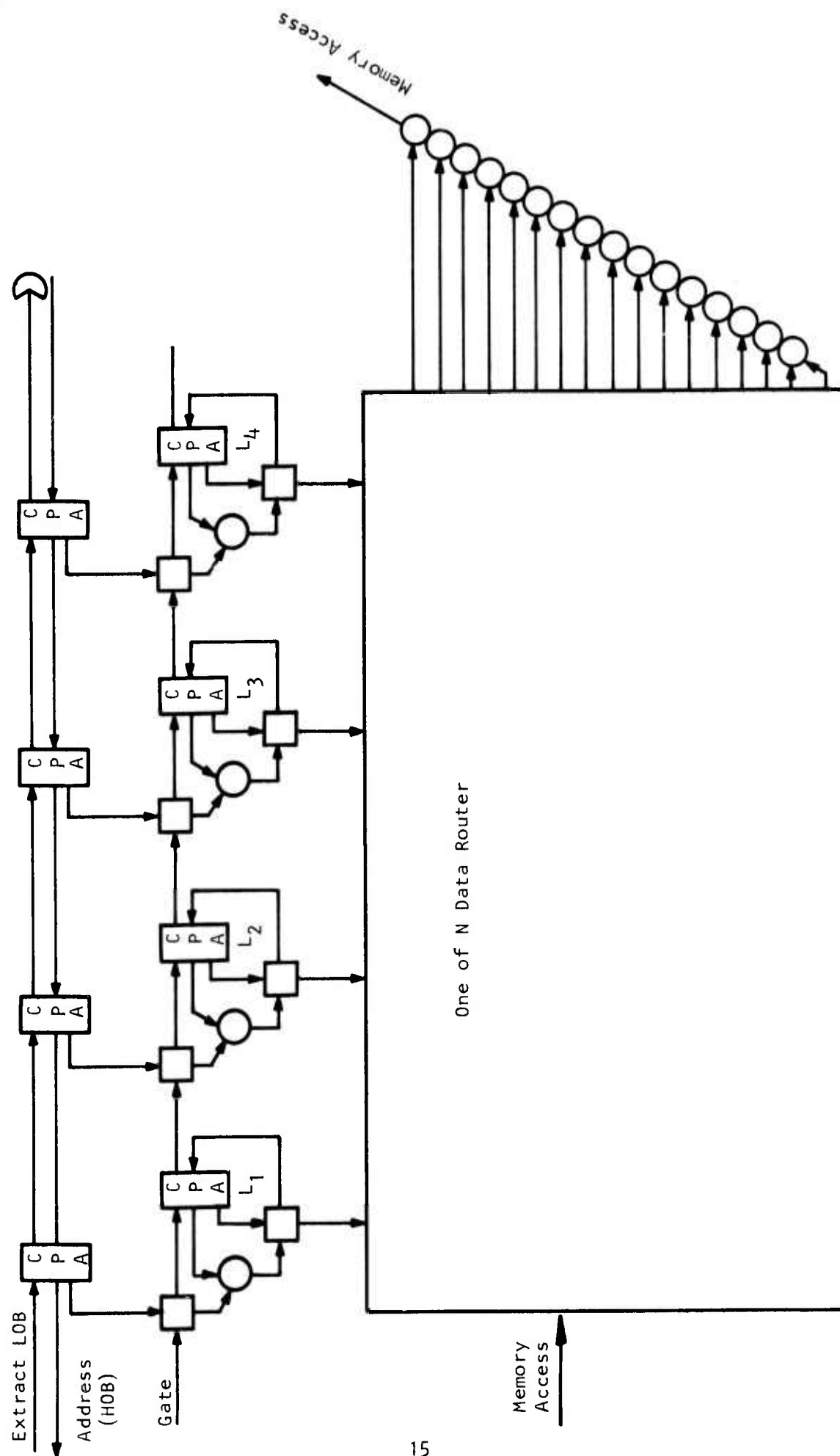


Figure 9 Memory Access Delay Network (Fine) Using Only Transient Bubble Logic

Figures 10 and 11 show a design for a memory access delay timer using resident bubble switch logic. The design is very similar to the previous design except that the data router is replaced by a variable delay circuit. This variable delay circuit is made possible by the asynchronous nature of the resident bubble switch.

Status Report No. 17 presents a discussion and preliminary comparison of three different bubble logic sets that can be used for performing logic functions. Also, implementations of a demultiplexer circuit and of the complete fast multiply circuit described in AFAL-TR-74-19 are given.

The term "logic element" refers to a specific bubble control function which must be performed on the chip. Such control functions can frequently be performed in more than one way. For example, bubble generation has been performed by (1) current-carrying conductors, (2) seed-bubble Permalloy generators, (3) pulsed laser radiation, or (4) a combination of (1) and (2). Keeping in mind the object of our investigation, an all-bubble (or mostly-bubble) processor, we require that as many of these functions as possible be performed by simple rotating field access. Thus, for Permalloy circuits the functions will be controlled by Permalloy elements of the appropriate nature and bubble-bubble interactions. The same requirements would also apply to other specific hardware implementations, e. g., ion-implant field access devices. Since it is not yet clear just what functions meet these requirements, alternative sets of logic elements are being considered.

Three candidate sets of bubble logic elements have now been examined. Each of these sets can, in principle, be used to implement any logic function. However, the resulting implementations have different degrees of complexity. To compare the relative complexity of these sets of logic elements, full-adder circuits which incorporate each of these element sets have been designed. These three designs are shown in Figures 12, 13, and 14. The input phasing of bubbles is represented by dashed circles.

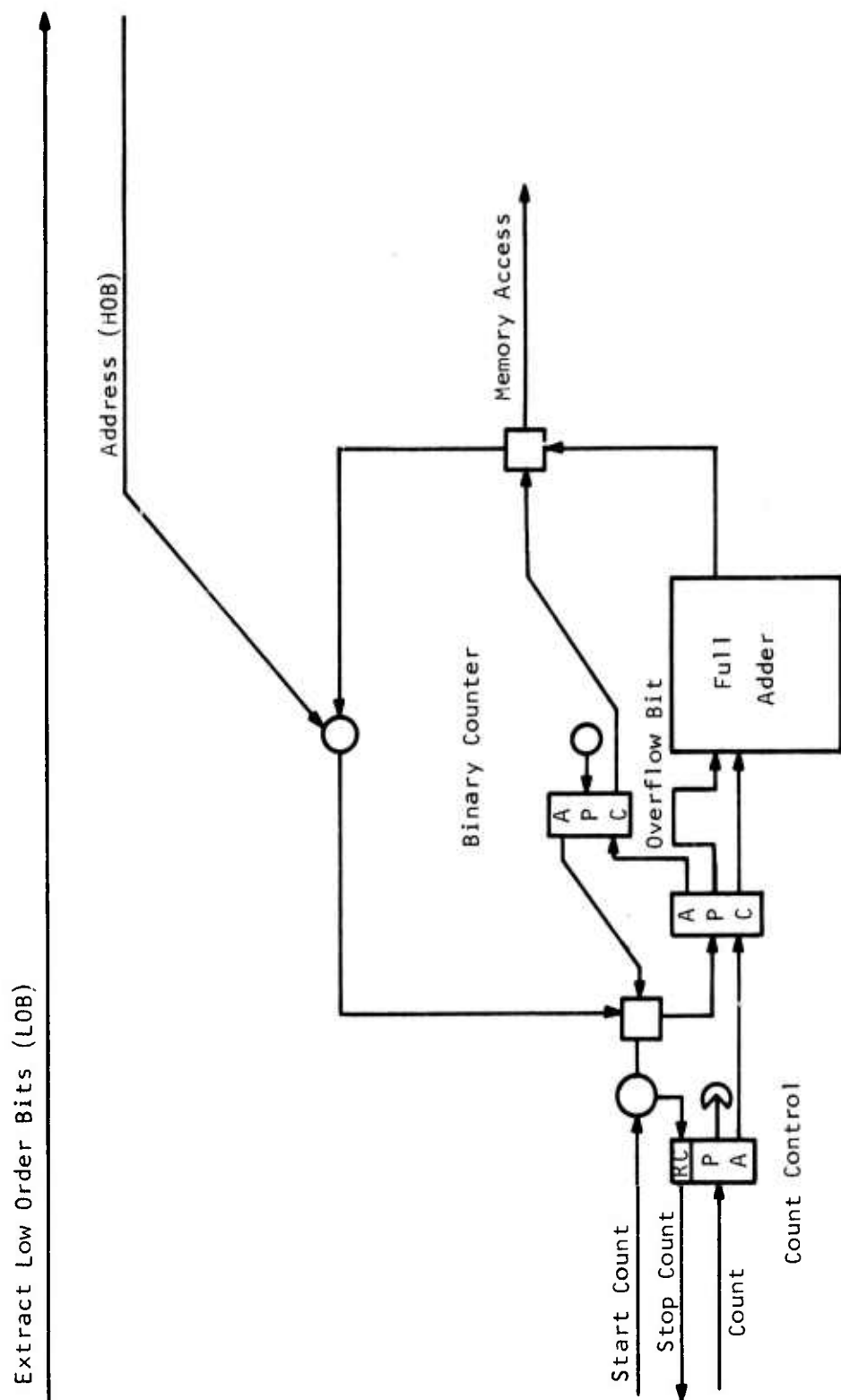


Figure 10 Memory Access Delay Network (Coarse) Using Resident Bubble Logic

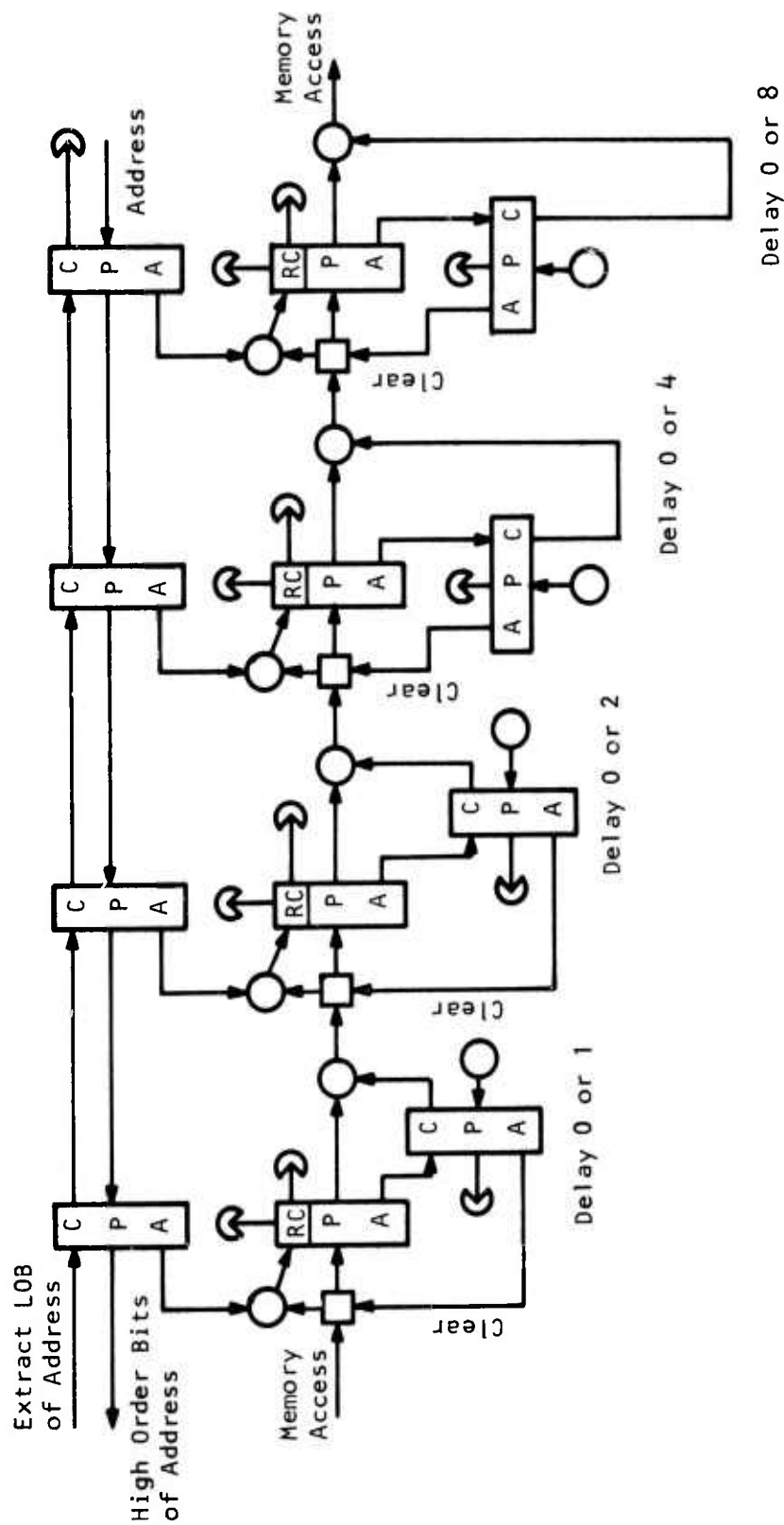
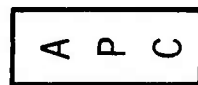
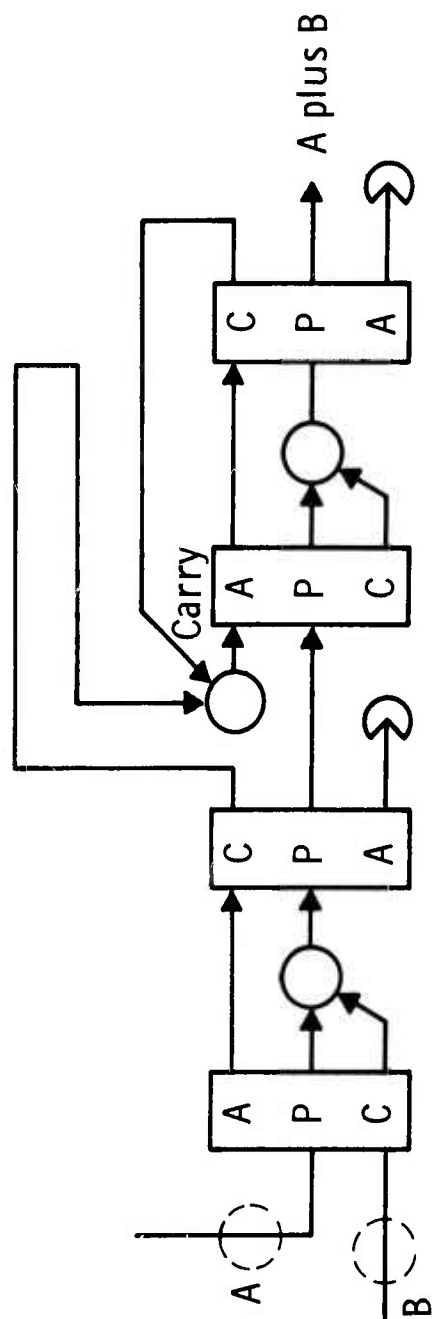


Figure 11 Memory Access Delay Network (Fine) Using Resident Bubble Logic



Transient Bubble Switch



Exclusive Merge

Figure 12 Full Adder Using Logic Set I Elements

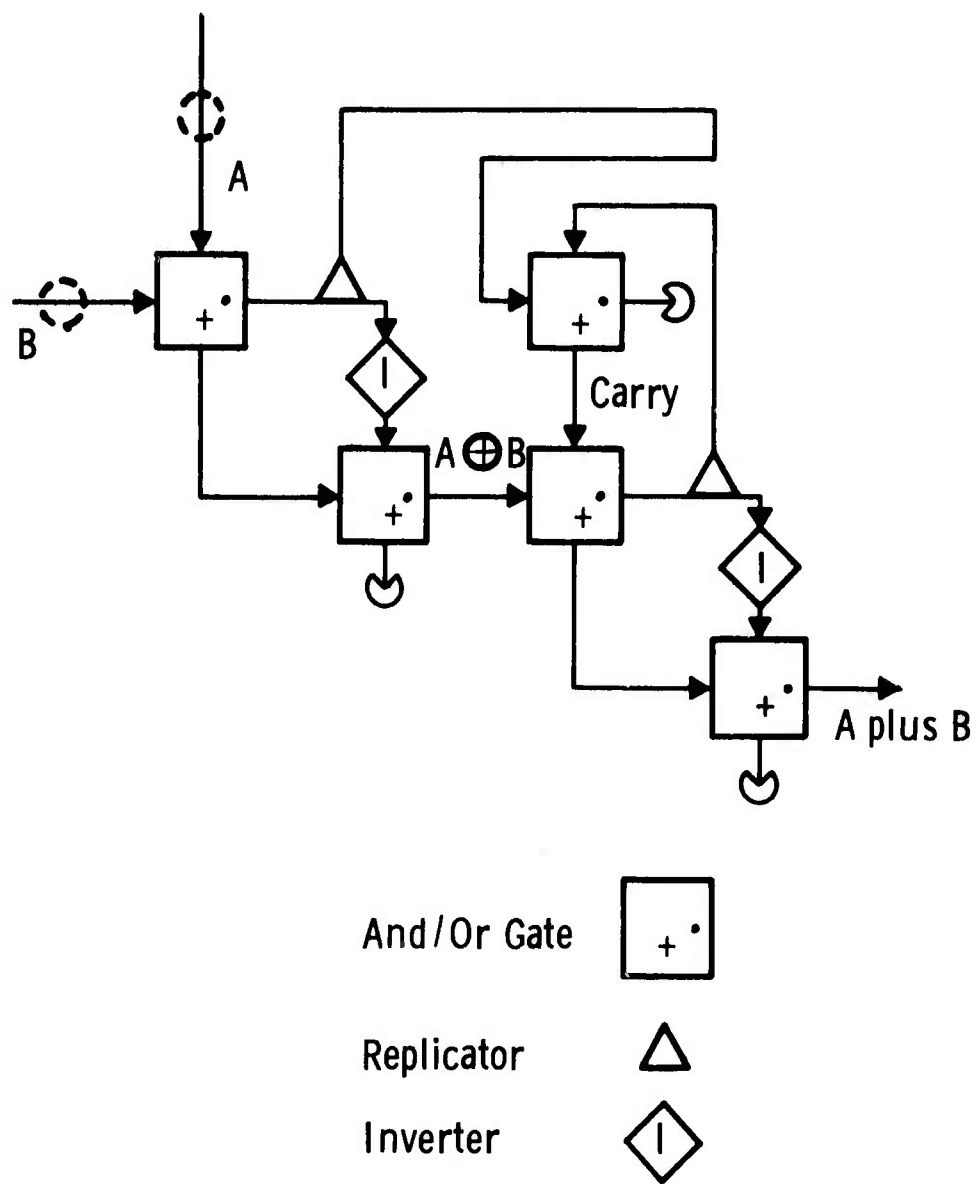
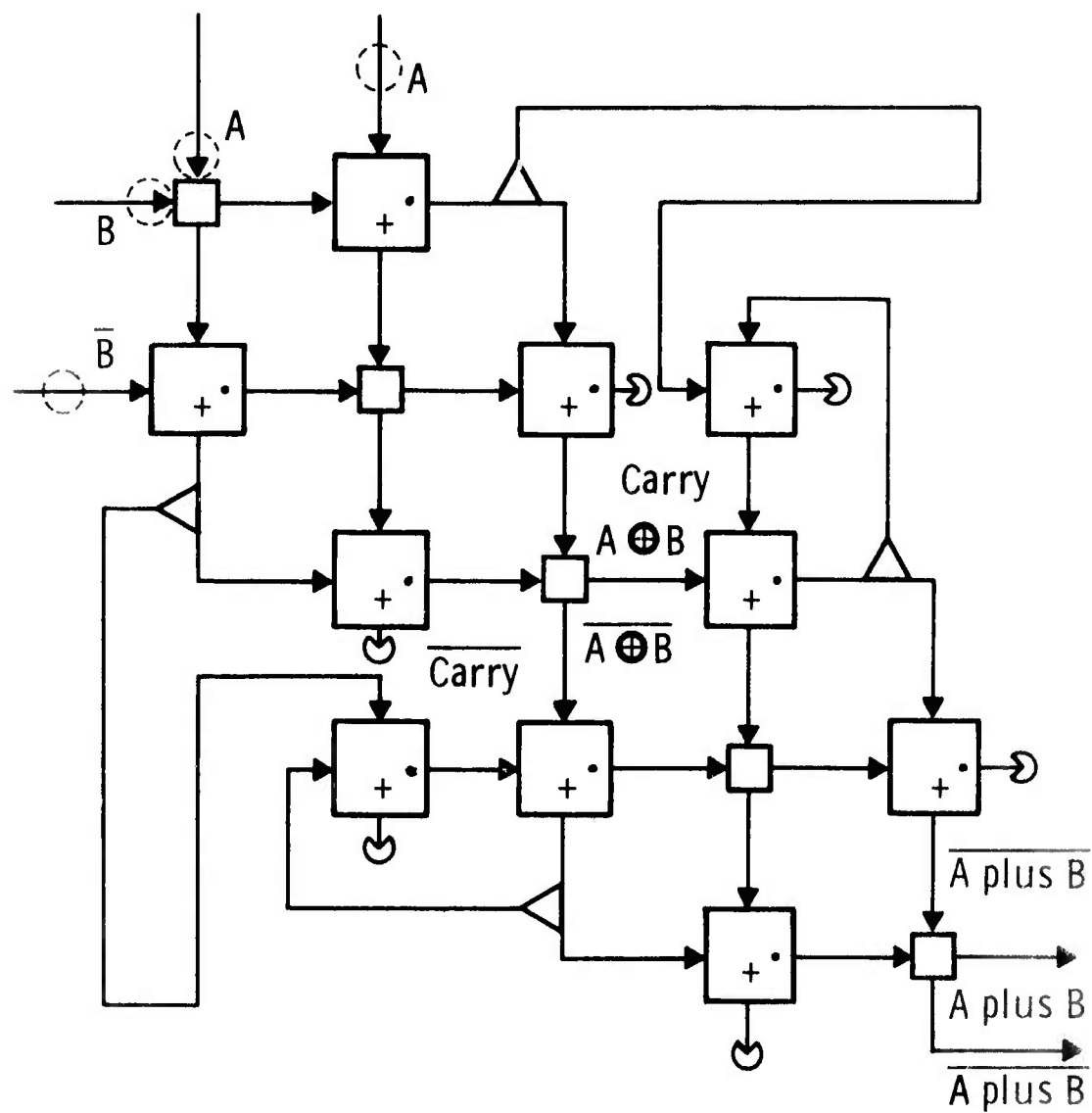




Figure 13 Full Adder Using Logic Set II Elements



And/Or Gate 

Crossover 


Replicator 

Figure 14 Full Adder Using Logic Set III Elements

The logic sets used for the full-adder design are listed in Table II. Logic Set I is based on the transient bubble switch described previously. Logic Set II is an analog of conventional electronic logic based on the AND/OR gate. Logic Set III is also based on the AND/OR gate, but assumes that a logical inverter is not available. Logic systems are constructed from Set III components so that a logical value and its complement are always available at each operation. The logical complement of a function is always produced along with the function. Inversion can then be performed by exchanging a logic value with its complement.

As an exercise to evaluate the relative complexity of systems constructed from the above sets of logic elements, a full-adder circuit was designed using each of the logic sets of Table II. The resulting complexity of the full-adder circuits is a good indication of the complexity that can be expected in general logic circuits.

Table III lists the number of logic elements used for each design. The full-adder using the transient bubble switch (Set I) uses the least number of components and has the simplest interconnection complexity, while the circuit designed using logic element Set III uses nearly three times as many components and has a much greater degree of interconnection complexity. The circuit designed using Set II falls between the other two in terms of complexity.

Assuming that the logic elements of all three logic sets can be built from Permalloy elements of comparable size, and that these elements operate with comparable operating bias field margins, Logic Set I is superior in terms of complexity, size, and speed of operation. However, hardware implementations of the transient bubble switch and the bubble logic inverter have yet to be accomplished. If these elements cannot be built, bubble logic will probably have to be implemented with Set III elements.

Table II

Three Candidate Sets
of Logic Elements

<u>Set I</u>	<u>Set II</u>	<u>Set III</u>
Generator	Generator	Generator
Annihilator	Annihilator	Annihilator
Disjoint Crossover	Disjoint Crossover	Disjoint Crossover
Exclusive Merge	AND/OR Gate	AND/OR Gate
Transient Bubble Switch	Inverter	Replicator
	Replicator	

Table III
Device Element Count for Full-Adder Circuits

<u>Circuit I</u>		<u>Circuit II</u>	
<u>Element</u>	<u>No. Required</u>	<u>Element</u>	<u>No. Required</u>
Generator	0	Generator	0
Annihilator	2	Annihilator	3
Disjoint Crossover	0	Disjoint Crossover	0
Exclusive Merge	3	AND/OR Gate	5
Transient Switch	<u>4</u>	Inverter	2
Total Elements	9	Replicator	<u>2</u>
		Total Elements	12

<u>Circuit III</u>	
<u>Element</u>	<u>No. Required</u>
Generator	0
Annihilator	3
Disjoint Crossover	5
AND/OR Gate	10
Replicator	<u>4</u>
Total Elements	22

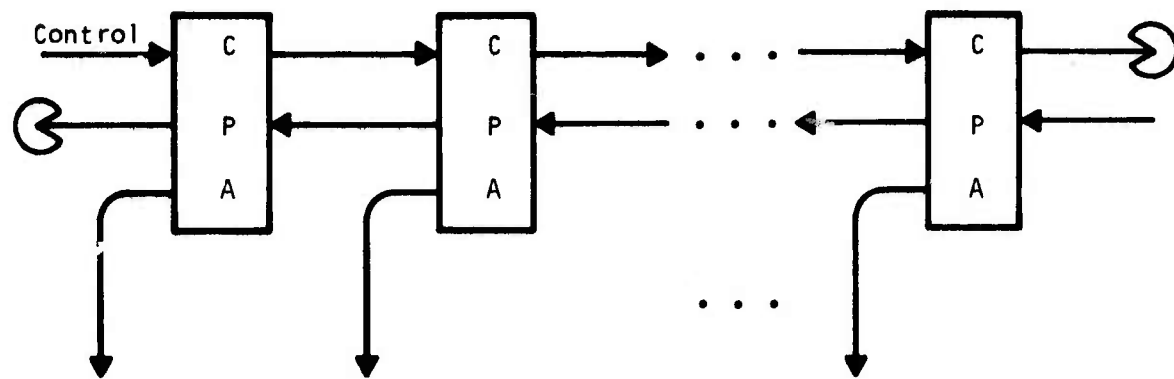
The demultiplexer, shown in Figure 15, takes a string of N sequential bubbles and converts them into a set of single bubbles, each traveling on one of N paths. The demultiplex operation is controlled by an input control bubble. This circuit is used to load the one-bit registers of the multiplier from a sequential bit string.

Designs have been completed for the demultiplexer and a fast multiplier. The multiplier operates on the convolution principle. The multiplicand is held in a register consisting of a set of closed bubble loops, each loop holding one bit, as shown in Figure 16. The multiplier is shifted sequentially by the multiplicand register, and the binary products of the adjacent bits of the multiplier and multiplicand are fed into a tree of full-adders, converting the product to standard binary form, as shown in Figure 17.

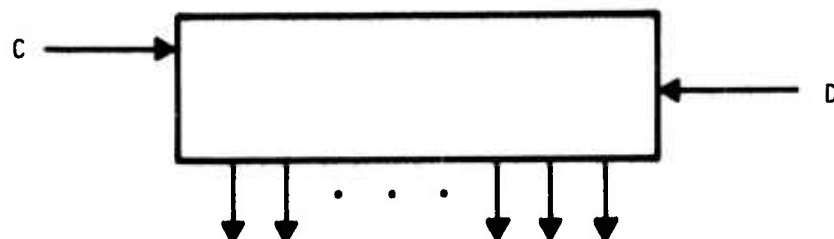
B. Status of One-Chip Bubble Processor Design

The only remaining functions to be designed are the instruction decode, control, and index register. The conceptual design of the bubble processor is expected to be completed by September 1974. From this functional design, assuming a particular Logic Set, we expect to provide the following information with regard to performance:

- The number of instructions per second.
- The chip size for a one-chip processor.
- Realizability in terms of implementable hardware.



Demultiplexer Detail



Demultiplexer Symbol

Figure 15 Demultiplexer Circuit

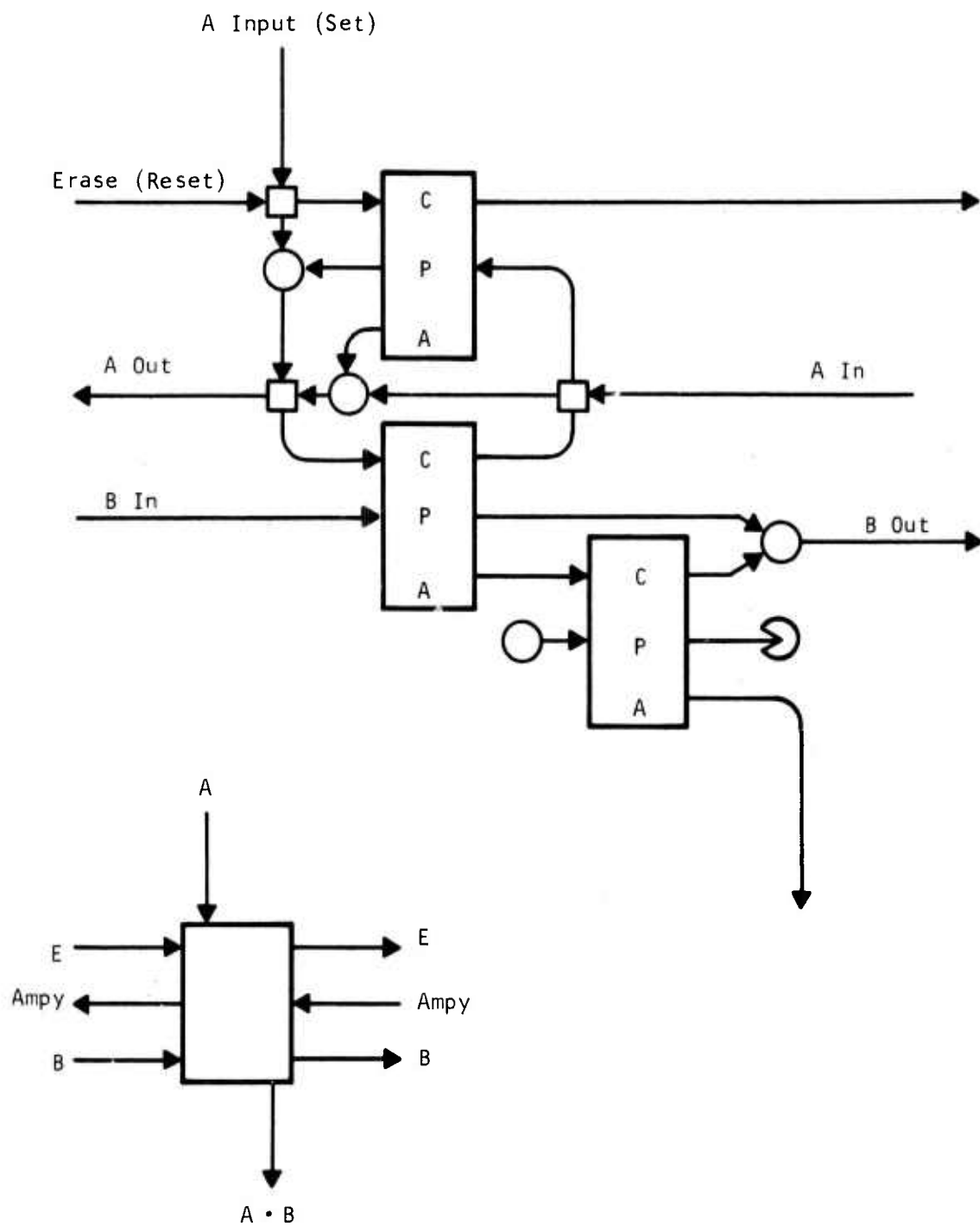


Figure 16 Storage Register

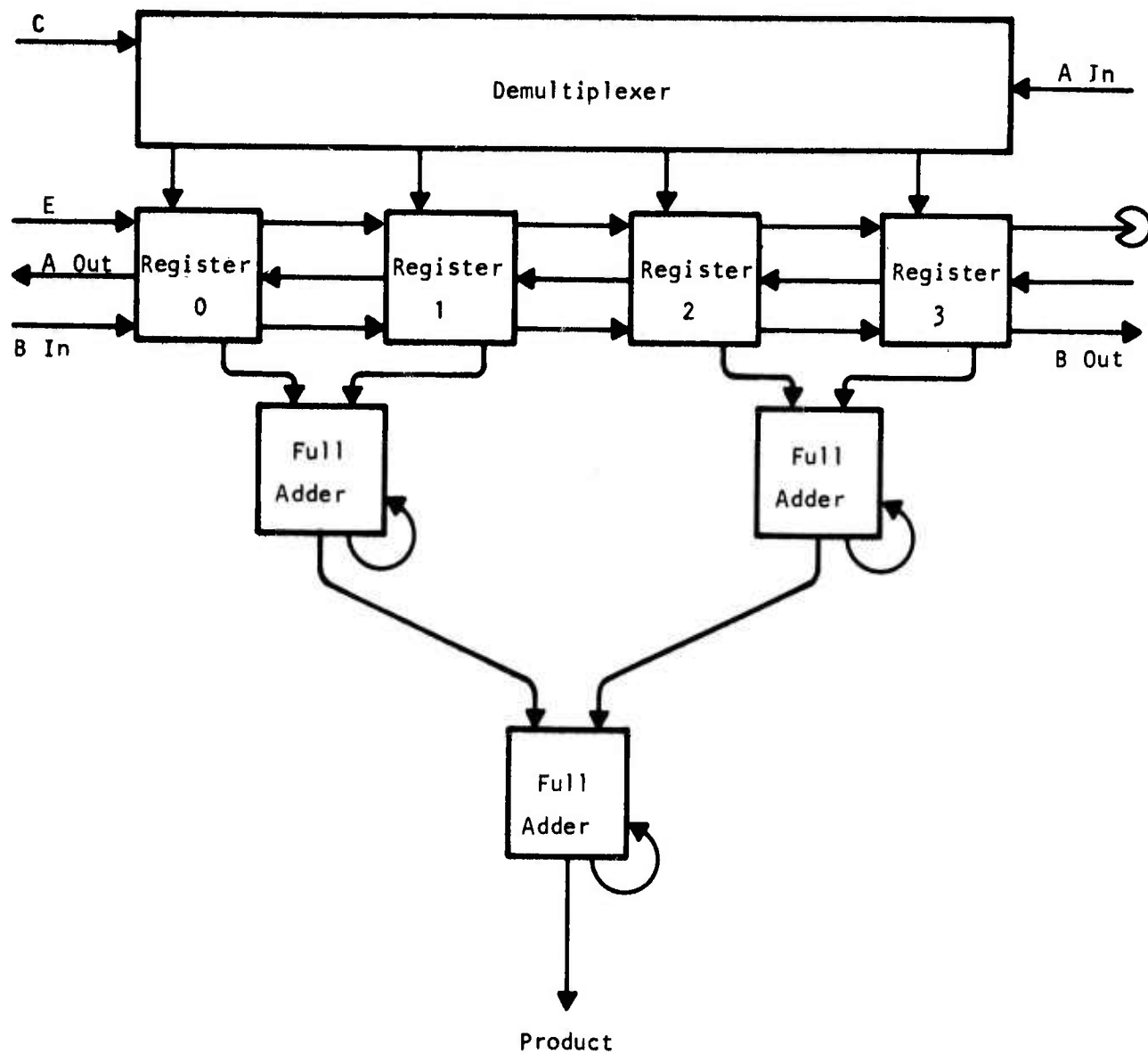


Figure 17 Fast Multiplier Circuit

SECTION II
PROGRESS ON TASK II, CONCEPTUALIZATION
OF HYBRID TECHNOLOGIES

A. Optical Waveguide Structures

1. Summary

Three integrated optic bubble detection configurations are now being investigated. As described in AFAL-TR-74-19, one configuration utilizes the epitaxial garnet film as the optical waveguide. Another configuration utilizes an ion implanted layer at the top surface of the film as the waveguiding medium. A third configuration which was defined during this last reporting period makes use of an internally reflected light beam propagating by internal reflection within the film/substrate composite. Experimental results on these three configurations are described in this report.

2. Experimental Results on Magneto-optic Modulation of Light Propagating by Internal Reflection

We have examined a bubble detection scheme which utilizes a magneto-optically modulated, internally reflected beam propagating in the garnet film/substrate composite. Figure 18 illustrates the internal reflection process; one notes that because the angle of the beam at the crystal-air interface is greater than the angle for critical reflection, the light is totally confined to the film/substrate composite. Thus θ , the internal reflection angle, defined in Figure 18, must be greater than 30.8° to obtain a totally reflected light beam. For θ less than this angle, the beam will exit from the composite film/substrate into the air.

As shown in Figure 18, the internally reflected beam passes through the bubble film at each reflection at the top surface. Because the refractive index difference between the bubble film and GGG is small, less than 10% of the light

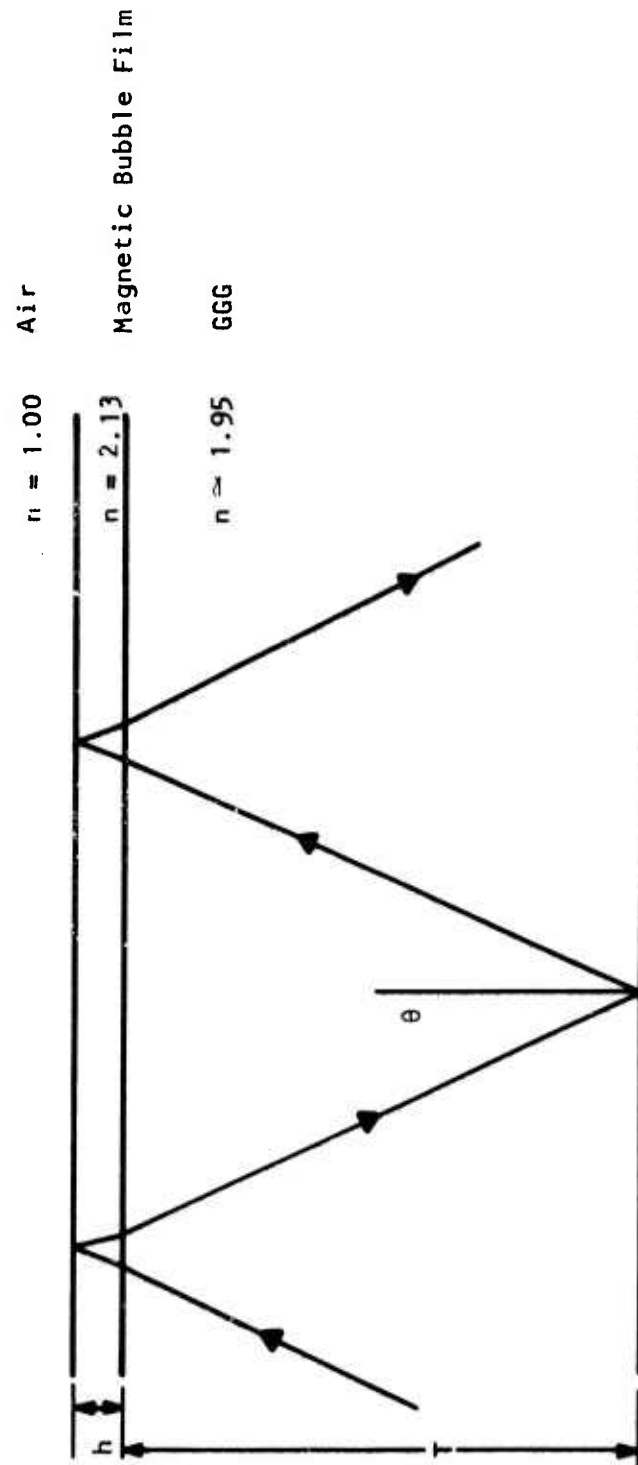


Figure 18 Geometry for Internal Reflection Inside the Composite Bubble Film/Substrate

is reflected at the film-substrate interface according to the Fresnel formulas.⁴ This reflected portion can be minimized by making the angle of incidence equal to the Brewster angle, which is about 47° for an internally reflected TE mode. The major part of the beam thus passes through the magnetic bubble film and back again. A Faraday rotation equal to $2\theta_F h$, where θ_F is the intrinsic Faraday rotation and h is the thickness of the bubble film, is given to the beam each time the beam passes through the film.

The experimental arrangement used to detect modulation by magnetic domains is shown in Figure 19. A 400 Hz magnetic field perpendicular to the plane of the sample was produced by a coil placed at the back of the sample. The composition of the bubble film was $\text{Y}_{2.6}\text{Sm}_{0.4}\text{Fe}_{3.9}\text{Ga}_{1.1}\text{O}_{12}$ and the thickness was $5.2\text{ }\mu\text{m}$. Figure 20 illustrates the percent modulation of the detected beam versus the amplitude of the ac magnetic field. The percent modulation is the ac detector signal divided by the detector dc level multiplied by 100. The x-axis intercept in Figure 20 is twice the coercive field, which for this sample is 0.3 oersted.

In this experiment, the laser beam diameter was 0.8 mm, and the light was reflected only one time at the upper surface, giving three passes through the film. The beam area extends over many domains, and the modulated signal is related to the average area of domains in the up or down direction. This average area is modulated by the ac magnetic field perpendicular to the film. The expected percent modulation, S , is given by:

$$S = 2 \sin (2\theta_F h' f) \times 100\%, \quad (1)$$

where θ_F is the Faraday rotation constant; h' is the effective light path (equal to $3h$ for the arrangement in Figure 19); and f is a parameter dependent on the

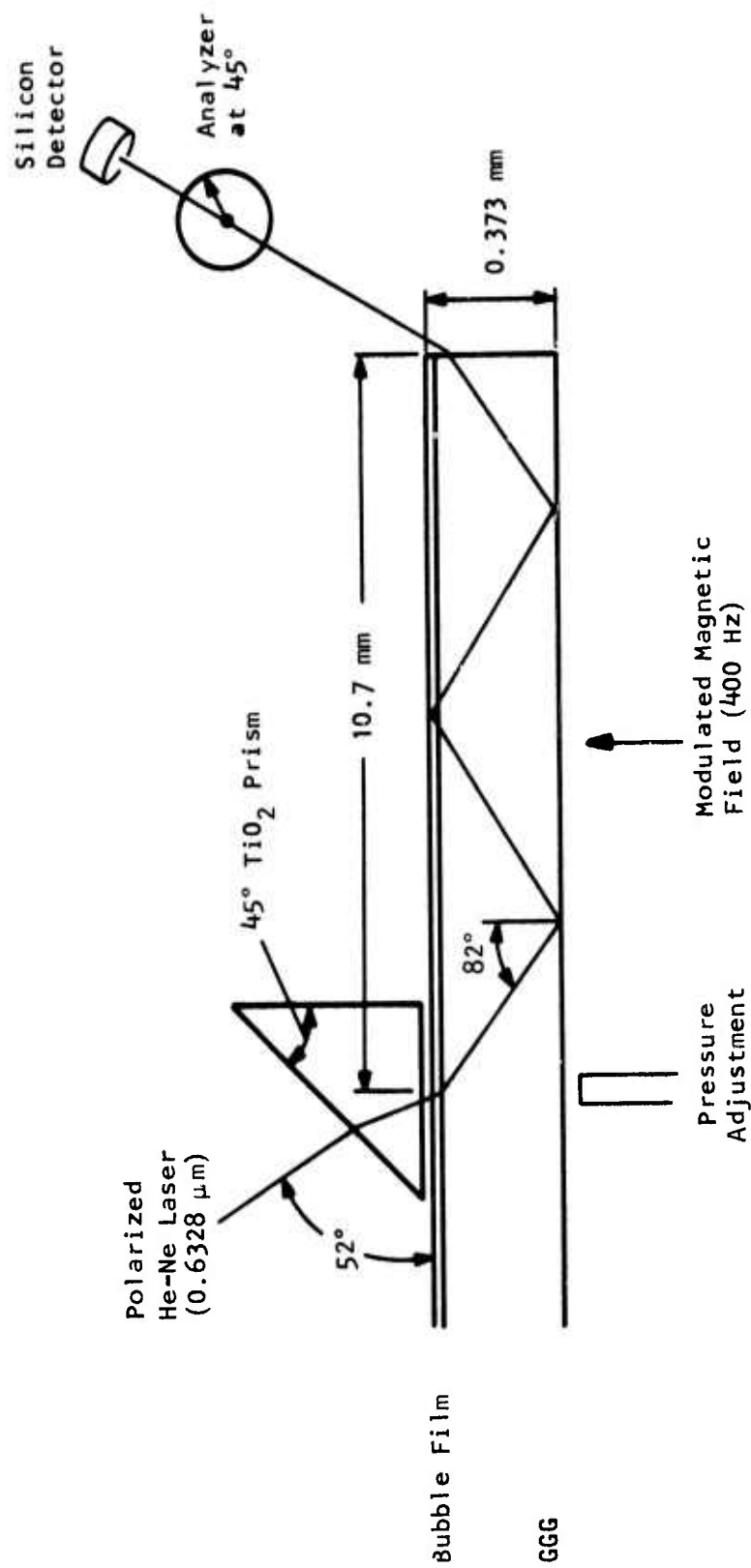


Figure 19 Experimental Optical Modulation Apparatus Using an Internally Reflected Beam

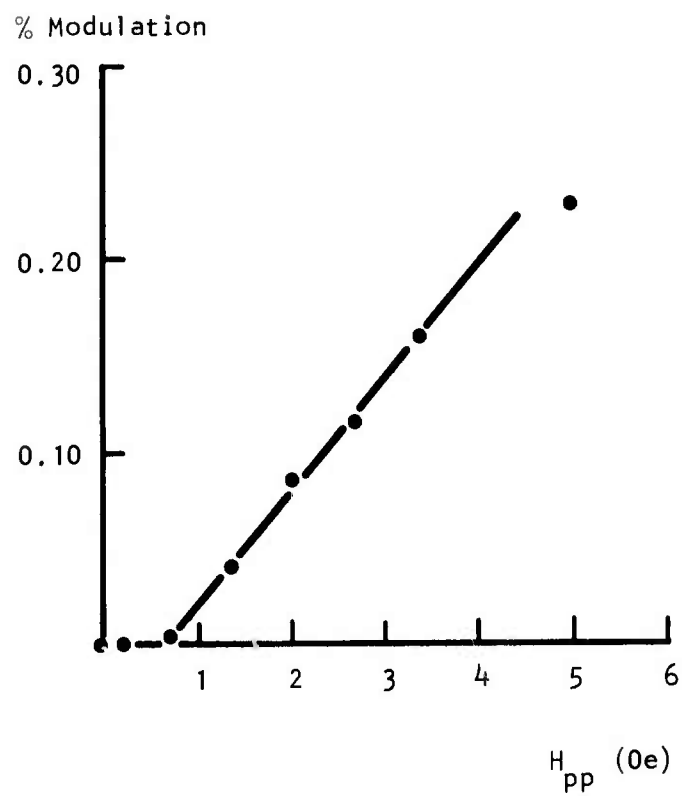


Figure 20 Percent Modulation Versus Magnetic Field Amplitude

fractional areas of the magnetic domains, having magnetization up and down. Note that $f = 1$ for a magnetic field large enough to completely saturate the sample.

For the configuration illustrated in Figure 19, with a peak-to-peak field, H_{pp} , of 4 Oe, we have determined that $f = 0.025$ by using an optical hysteresigraph to measure net magnetization versus applied field. Thus, for $h = 5.2 \mu\text{m}$, and $\theta_F \approx 1000^\circ/\text{cm}$, we calculate $S = 0.27\%$. This calculated value of S is in good agreement with the experimental value of 0.2%. These results can now be used to estimate the efficiency of a detector based on optical modulation by a "stretched" bubble when light propagates by internal reflection. Subsequent work will compare this detection method with the others now under investigation.

3. Experimental Results on Waveguiding Confined to the Garnet Film

Optical waveguiding and magnetooptic modulation at $1.15 \mu\text{m}$ in a magnetic garnet film deposited on a GGG substrate were observed during this reporting period.

A rutile prism (TiO_2) was used to couple the light from a 1 mW He-Ne laser source operating at $1.15 \mu\text{m}$ into the film. A Metascope (S-1 photomultiplier) was used to align the input coupling prism and the laser to observe the waveguiding. No bright scattering of the light at film imperfections, often characteristic of waveguiding, was observed. However, a bright spot was observed at a scratch purposely scribed into the film surface to intersect the guided beam. The absence of scattering in the unscratched film illustrates that the bubble film is of high quality and is suitable for low loss optical transmission. Scattering at the scratch is evidence of waveguiding in the film.

As reported in Status Report No. 17, we also have now observed the characteristic m-lines⁵ in films. These lines are experimentally observed at the synchronous angles of the input light beam for which waveguiding occurs. The m-lines are observable at 0.6328 μm and 1.15 μm . Besides giving experimental confirmation of guiding, they can be used for accurate determination of the refractive index and thickness of a garnet film. Table IV lists the synchronous angles for a 5.3 μm thick, $\text{Y}_{2.6}\text{Sm}_{0.4}\text{Fe}_{3.9}\text{Ga}_{1.1}\text{O}_{12}$ film deposited on a GGG substrate. The experimental configuration for measuring these angles is illustrated in Figure 21.

At the synchronous angles for 0.6328 μm radiation only a single spot with a dark line through the center is observable. For 1.15 μm radiation the side lines corresponding to intermode coupling are observable, but weak. At 0.6328 μm the dark line is easily observable, since light coupled into the film is lost by scattering before the light couples out of the film. At 1.15 μm , on the other hand, the dark line is weak and difficult to observe because the light coupled into the film (which is transparent at this wavelength) is not absorbed and couples out. To enhance this line we carefully adjusted the prism-to-film spacing so that this gap increased to the right of the laser focal point. Thus, the light coupled into the guide did not completely couple out, and we observed both a dark line on the screen and a bright spot at a scratch in the film intersecting the guided wave. To observe the side lines on the screen corresponding to mode coupling, an ion implanted film was utilized. The scattering of the guided beam by the implanted layer permitted a small amount of intermodal conversion. Further properties of the ion implantation process will be given in Section II.A.4, "Experimental Results on Ion Implanted Waveguides."

At the time this report is being written we have just made our first qualitative observations of magnetooptic modulation (at 1.15 μm) of radiation

Table IV
Synchronous Angles for TE Modes

<u>Wavelength</u>	<u>θ_s</u>		<u>β/k</u>
0.6328 μm	51°	2'	1.955 ± 0.003
	48°	51'	1.982
	46°	45'	2.010
	44°	43'	2.030
	42°	58'	2.057
	41°	8'	2.078
	39°	37'	2.095
	38°	8'	2.110
	36°	42'	2.128
1.15 μm	42°	39'	1.938 ± 0.005
	39°	29'	1.976
	36°	36'	2.010
	33°	58'	2.040
	31°	43'	2.065
	29°	50'	2.085
	27°	19'	2.112

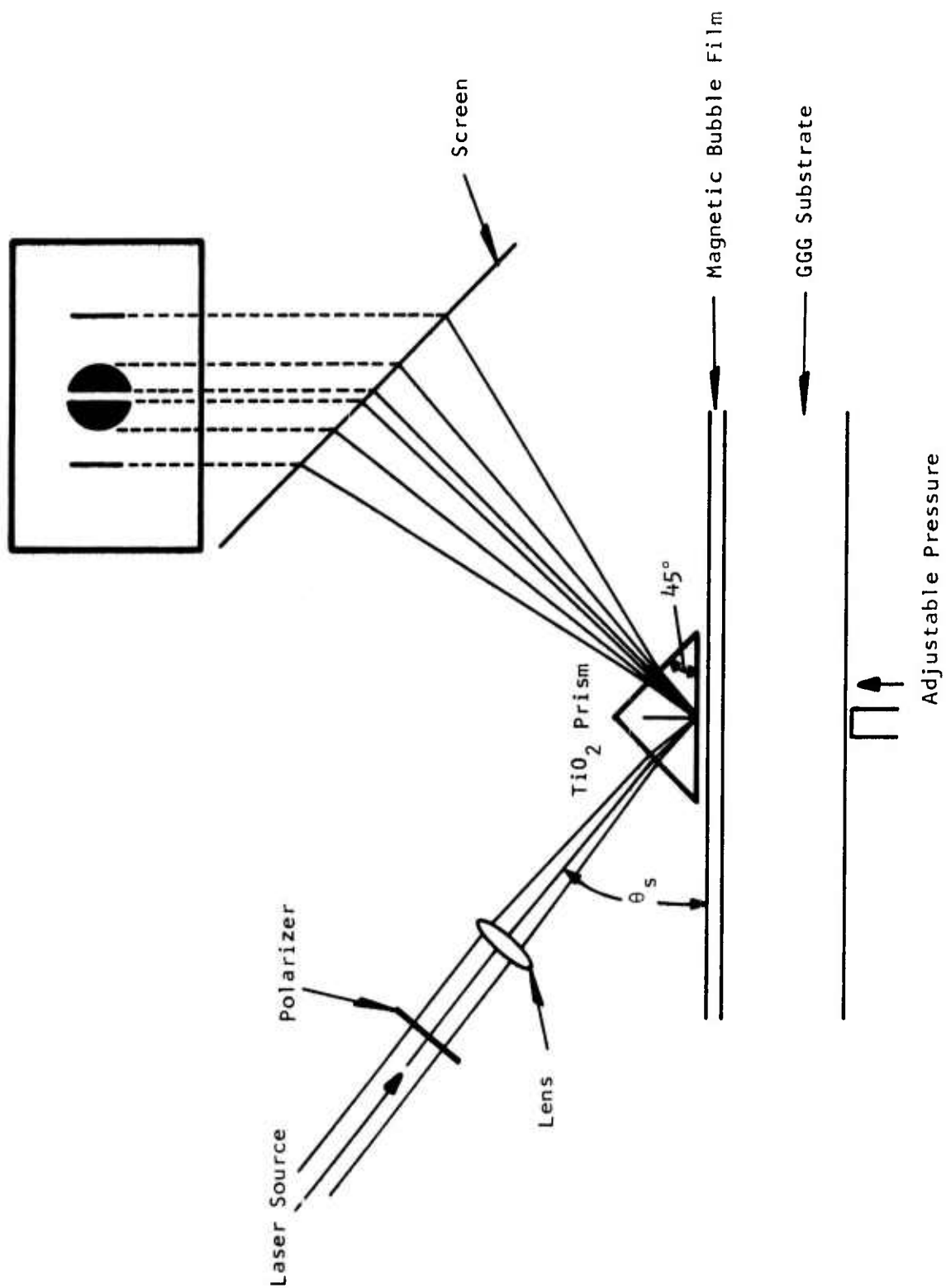


Figure 21 Experimental Arrangement for Observation of m-Lines

confined to guiding in a garnet film. Modulation by magnetic domains was achieved by applying an ac field in the manner described in the preceding section. Quantitative measurements will be made for comparison with the results obtained by the internal reflection arrangement.

4. Experimental Results on Ion Implanted Waveguides

Work is continuing on finding the right ion species and dosage to permit guiding in an ion implanted layer. While we have observed an index change produced by implantation, as of the writing of this report, waveguiding within an implanted layer has not been observed. Preliminary experiments were directed toward implanting GGG and attempting to observe guiding at $0.6328\ \mu\text{m}$ in this material. A triple dosage of Ne^+ ($2 \times 10^{15}\ \text{cm}^{-2}$ at 50 keV, 100 keV, and 150 keV) did not produce a guiding layer, although the implanted region appeared darker than an adjacent unimplanted region. Another dosage of Ne^{2+} with $4 \times 10^{15}\ \text{cm}^{-2}$ at 200 keV still did not produce a guiding layer. The use of Ne^{2+} is equivalent to a 400 keV dosage for Ne^+ and should result in a deeper ion penetration.

Because no guiding was observed for these dosages, we implanted garnet films instead of GGG substrate material. The presence of the iron ions in garnet films could enhance the refractive index change over that produced in GGG material, as a result of the sensitive charge compensation mechanism characteristic of the iron garnets.

Although we have not demonstrated guiding solely in the ion implanted layer, we have observed a shift in the m-line synchronous angles at $0.6328\ \mu\text{m}$ in the implanted region. This shift is due to an increased optical thickness of the garnet film caused by an increase, ϵ , in the refractive index in the implanted region. Figures 22(a) and 22(b) illustrate the implanted region and an unimplanted region. Symbols used below are defined in these figures.

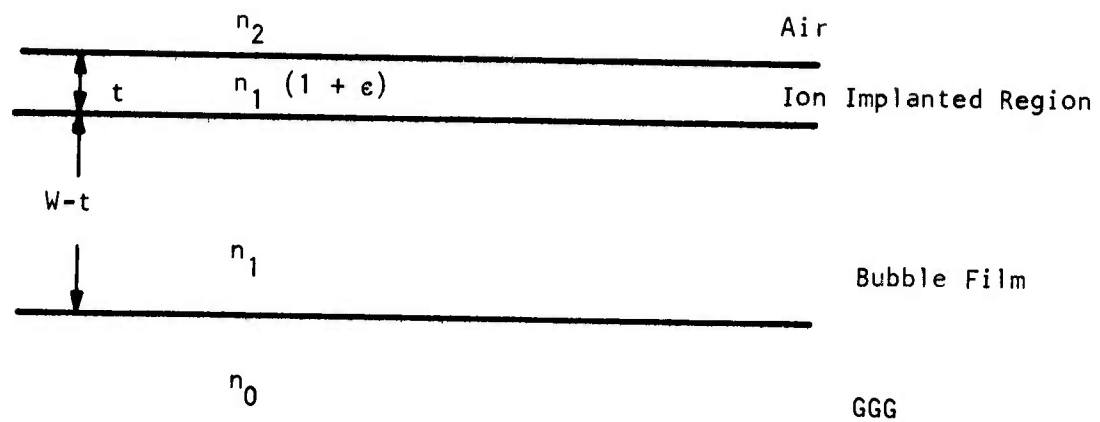


Figure 22(a) Implanted Film Geometry

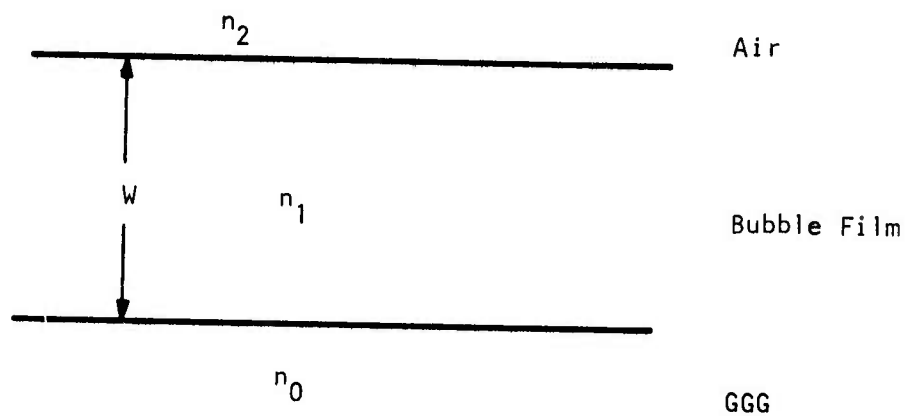


Figure 22(b) Unimplanted Film Geometry

The m-line shift due to the ion implanted layer is calculated using the waveguide TE mode equation⁶ for an optical waveguide:

$$b_1 W - \phi_{10} - \phi_{12} = m \pi ; \quad (2)$$

where $\tan \phi_{10} = p_0/b_1$,

$$\tan \phi_{12} = p_2/b_1 ,$$

$$b_1 = \sqrt{(kn_1)^2 - \beta^2} ,$$

$$p_0 = \sqrt{\beta^2 - (kn_0)^2} ,$$

and

$$p_2 = \sqrt{\beta^2 - (kn_2)^2} .$$

In these relations m is an integer corresponding to the mode number; k is the free-space wave vector; β is the propagation constant in the unimplanted layer; and W is the guide thickness as shown in Figure 22(b).

For the implanted region, shown in Figure 22(a), assuming a small refractive index change ϵ of the implanted region, Equation (2) becomes:

$$b_{1i}(W-t) + b'_{1i}t - \phi_{10} - \phi_{12} = m \pi , \quad (3)$$

where: $b'_{1i} = \sqrt{[kn_1(1 + \epsilon)]^2 - \beta_i^2} ,$

$$b_{1i} = \sqrt{(kn_1)^2 - \beta_i^2} ,$$

and the subscript i refers to the implanted structure. Solving Equations (2)

and (3) for the same m , one obtains:

$$\epsilon t = \frac{b_{1i} [b_1 - b_{1i}] W}{(kn_1)^2} . \quad (4)$$

Calculation of the b_{1i} which is related to the synchronous angles in the implanted region and b_1 in the unimplanted region of the same sample, for the same mode number, determines ϵt from Equation (4).

As an example, a $7.2 \mu\text{m}$ thick $\text{Y}_{2.6}\text{Sm}_{0.4}\text{Fe}_{3.9}\text{Ga}_{1.1}\text{O}_{12}$ bubble film was implanted with Ne^+ at 50 keV, 100 keV, and 150 keV at a dosage of $2 \times 10^{15} \text{ cm}^{-2}$. A $0.6328 \mu\text{m}$ laser was focused onto the sample near the implanted-unimplanted interface using the m-line experimental arrangement shown in Figure 21. By shifting the beam spot between the two regions, a shift in the synchronous angle of 9° was observed. After determining b_1 and b_{1i} from the above definitions and substituting into Equation (4), one finds that $\epsilon t = 0.0056 \mu\text{m}$ for the ion implanted region.

From the theory of optical waveguides, Namba, et al.,⁷ have shown that the minimum refractive index change in an implanted region in order to have waveguiding solely in this region is approximately

$$\epsilon = \frac{1}{32n_1^2} \left(\frac{\lambda}{t} \right)^2 . \quad (5)$$

This equation applies for ϵ small and a homogeneous refractive index. For the implanted waveguide, the refractive index varies with depth into the sample.

The derivations of Equations (4) and (5) still apply if an effective ϵ and t are used for the waveguide mode calculation.⁷ Substituting the appropriate values ($n_1 \approx 2.13$, $\lambda = 0.6328 \mu\text{m}$) into Equation (5) yields $\epsilon t \approx 2.8 \times 10^{-3}/t \mu\text{m}^2$ as the minimum refractive index-thickness product to observe waveguiding. A typical value of t for an ion acceleration voltage of 150 keV is about $0.5 \mu\text{m}$. Thus, $\epsilon t > 0.006 \mu\text{m}$ for waveguiding to occur. Comparing this value with the calculated ϵt of $0.0056 \mu\text{m}$ for the example considered above, we conclude that this sample will not support a guided wave, and no m-lines attributable to guiding solely in the implanted layer have been observed experimentally. We will implant heavier dosages and higher energies during the next reporting period to increase ϵt still further and to confine guiding solely to the implanted layer. Evidence for this effect will be the observation of a separate series of m-lines.

Although we may obtain guiding in the implanted region at $0.6328 \mu\text{m}$, because of the high absorption at this wavelength, this effect is not useful for a bubble detection scheme. Instead, we plan to use the implanted waveguide at $1.15 \mu\text{m}$ to demonstrate magneto-optical modulation by domains using the scheme proposed in AFAL-TR-73-306. At this wavelength, a higher value of $\epsilon t \approx (9.1 \times 10^{-3})/t \mu\text{m}$ is required according to Equation (5). Again assuming $t \approx 0.5 \mu\text{m}$, $\epsilon t > 0.018 \mu\text{m}$ is required for guiding to occur.

B. Bubble/Elastic Wave Interactions

1. Experimental Observation of Stripe Domain Interaction with Bulk Elastic Waves

In AFAL-TR-74-19 an experiment designed to measure the effect of bulk elastic waves on the mobility of magnetic bubbles was described. In this configuration elastic waves travel normal to the film plane. Modifications have been made to the original experimental arrangement. Ceramic (PZT-5) transducers were substituted for the original quartz transducers to obtain larger strain amplitudes.

In addition, it was found that pulsed mode operation was necessary to avoid undue sample heating. Radio frequency acoustic pulses are now supplied by a Matec pulse generator (model 6000 mainframe with model 960 plug-in). The series resonant tuned circuit described in AFAL-TR-74-19 is not capable of driving the low impedance ceramic transducers to sufficient amplitude. Finally, an epoxy bond (Emerson and Cuming, Inc., Stycast 1266) was used to couple the acoustic waves across the transducer-garnet interface.

Observations of the displacement of stripe domains by acoustic waves in $(\text{YGdTi})_3(\text{GaFe})_5\text{O}_{12}$ films were made with this experimental arrangement. For these observations, the garnet films were biased by the dc magnetic field so that the initial serpentine domain pattern was considerably thinned out to leave only a few remaining loop domains. In this range of bias field, small increments of the bias field have the effect of increasing or decreasing the loop length.

It was found that the application of an acoustic pulse subsequent to such a field increment produced an additional change in loop length. Initially, we ascribed this behavior to domain/elastic wave coupling. Subsequent experiments, however, showed that the stray rf field surrounding the transducer assembly was responsible. This result indicates that the elastic strain in the acoustic pulse is lower than anticipated. We are somewhat puzzled by this and will attempt to determine if it is a question of strain amplitude or the wrong strain components which do not couple efficiently to the domain walls.

2. Surface Wave Interactions

A bubble propagation concept employing surface elastic waves was presented in AFAL-TR-74-19. Essential to this concept is the requirement for large strain amplitudes. We have experimentally examined the wedge technique for generating surface waves. This technique is analogous to the prism coupling technique used in integrated optics. Bulk waves are generated by a transducer and

coupled through an "acoustic prism" to the sample to be studied. Mode conversion at the sample-wedge interface generates the surface waves. This technique has the advantage of simplicity for initial investigations. However, we have not yet been able to generate strain amplitudes large enough to give an observable influence on bubble domains. The primary difficulty appears to be the large losses associated with the acoustic bond interfaces and mode conversion. To minimize these losses, the wedge angle and bonding procedure must be optimized. Several different wedges have been fabricated and are now being characterized.

SECTION III

PROGRESS ON TASK III, EXPERIMENTATION TO ESTABLISH PERFORMANCE OF INDIVIDUAL DEVICE ELEMENTS

A. Logic Hardware

1. Bubble Switch

In the last technical report, a set of logic elements based on a bubble switch [see Figure 23(a)] was reported. This set includes the bubble Generator, Annihilator, Switch, Exclusive Merge, and Crossover. It was used to realize several computer functions conceptually and was demonstrated to be both powerful and convenient to the system designers. To realize the switch function on the Permalloy element level in a field access device, two bubbles must maintain their separate paths. Moreover, the path of one bubble is diverted to an adjacent path according to the presence or absence of the other bubble. Since the radius for reliable bubble-bubble interaction across a Permalloy gap is found to be less than one bubble diameter, the task of forming three adjacent Permalloy paths in an area of approximately one bubble diameter is technologically difficult.

A bubble AND/OR gate (Figure 24) recently reported by Bonyhard, Chen, and Smith⁸ is essentially the bubble switch of Figure 23(a) with the two output paths, A and $\bar{A}B$, combined [see Figure 23(b)]. Ways to split these two output paths (i.e., A + B into A and $\bar{A}B$) have not been found. Moreover, a different set of logic elements based on the AND/OR gate can be chosen to perform all logic functions in a computing system. This set, described in Section I, includes the Generator, Replicator, Annihilator, AND/OR gate, Inverter, and Disjoint Crossover.

2. The AND/OR Gate

AND/OR gate circuits based on the design of Bonyhard, et al., (Figure 24) were fabricated on $(YSm)_3(FeGa)_5O_{12}$ at Texas Instruments. This circuit uses a

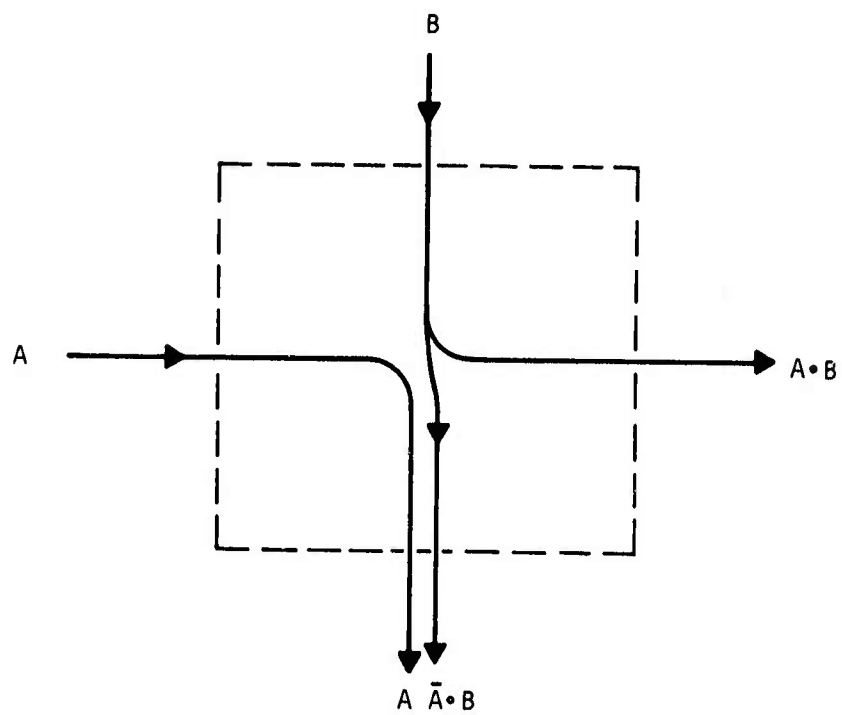


Figure 23(a) Bubble Switch

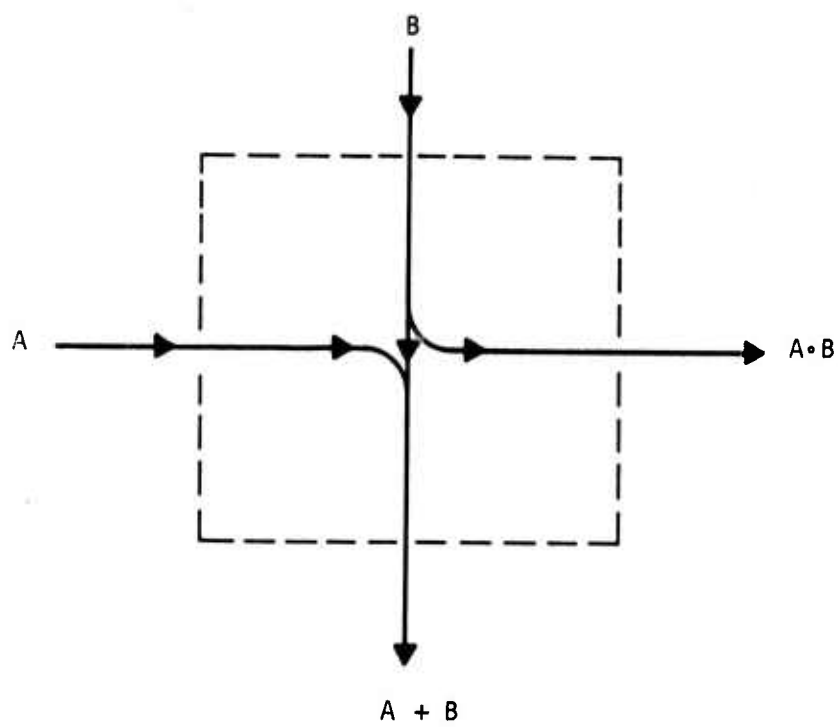


Figure 23(b) AND/OR Gate

AND/OR LOGIC GATE

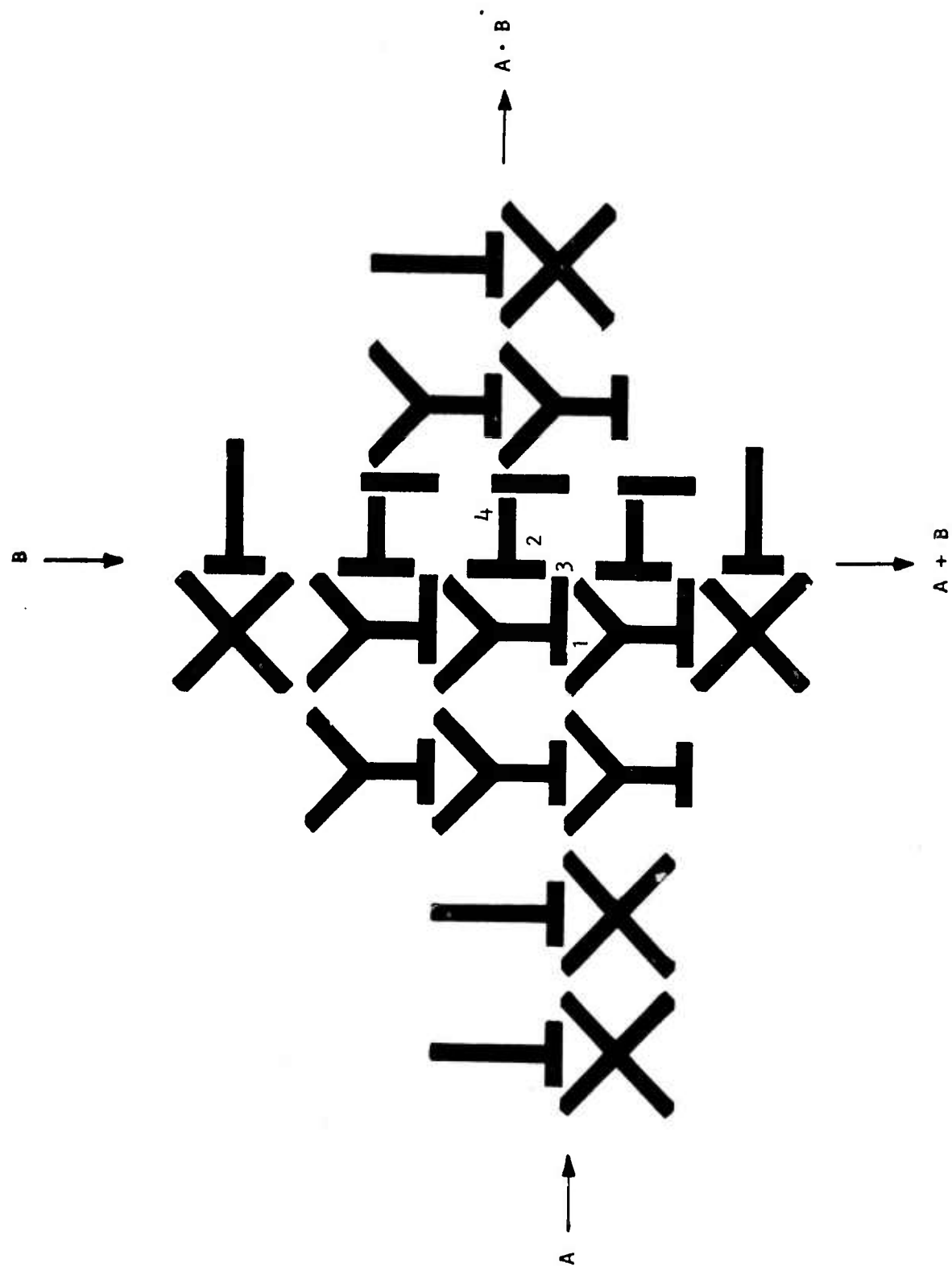


Figure 24 Permalloy AND/OR Gate

new propagating element, the TX, and a logic interactor, the TY. Bubbles enter the gate from the two inputs labeled A and B at the left and at the top of Figure 24. When there is only one input bubble in the interacting region, this bubble goes through point 3 and ends up at the $A + B$ output (at the lower part of Figure 24). However, the simultaneous appearance of bubbles at points 1 and 2 causes these bubbles to compete for point 3. The bubble from the A input finally prevails and occupies point 3. The repulsive force between the two bubbles deflects the B bubble to point 4, resulting in bubble outputs at both $A + B$ and $A \cdot B$ outputs.

Our first devices of this type were found to have 6 to 7 Oersted bias field margins for quasistatic operation. However, the larger than usual gaps between the TX propagation elements degrades the bias field margin at 100 kHz to an unacceptable level. A modified AND/OR circuit with narrowed gaps has been submitted for photomask fabrication. This new design will hopefully provide an acceptable bias field margin.

3. Other Logic Elements

As previously stated, other elements are required before an all-bubble processing unit can be realized. Among these elements, the current-pulsed bubble generator and the replicator/annihilator have been developed in conjunction with our work on memory circuits. The bubble inverter, which converts the presence (or absence) of a bubble at the input into its complement at the output, has not yet been devised. However, the essential inverter function can be fulfilled by operating a pair of bubble generators from the outputs of an electronic flipflop, storing these bubbles, and carefully routing them to the locations where the inverted bubble signals are required.

A crossover element that allows two bubble tracks to cross each other was conceived. Several variations of this element have been designed and submitted for photomask fabrication. One of these designs is shown in Figure 25. Bubbles from two separate tracks pass through the crossover region at different times within one drive field clock cycle. The resulting spatial separation of bubbles from different tracks minimizes bubble-bubble interaction at the crossover and enables the bubbles to travel along their respective paths.

Finally, a preliminary Permalloy design for a complete Full-Adder circuit based on this set of logic elements (Set II, Table II, Section I) was laid out to determine to what extent it is practical. While this logic set is wasteful of chip area due to the necessity for carrying along the complement of the data stream, it does appear to be possible to route the data paths through the logic elements in a rather direct manner. Therefore, if each of the logic elements can be made to operate with acceptable bias field margins, a practical circuit should be possible. Pending successful demonstration of acceptable AND/OR and Crossover elements, Permalloy Full-Adder circuits will be fabricated for demonstrating practical logic.

B. Small Geometry Permalloy Circuits for Submicrometer Diameter Bubbles

1. E-beam Patterning and Device Processing

E-beam circuit patterning has progressed rather well during this reporting period. Our ability to pattern large-area T-bar circuits with $2.4\text{ }\mu\text{m}$ periods and 0.3 to $0.4\text{ }\mu\text{m}$ linewidths has continued to improve. Arrays of chevrons were also patterned.

Techniques for compatible device processing were also developed during this period. A sequence of processing steps has been developed for Permalloy

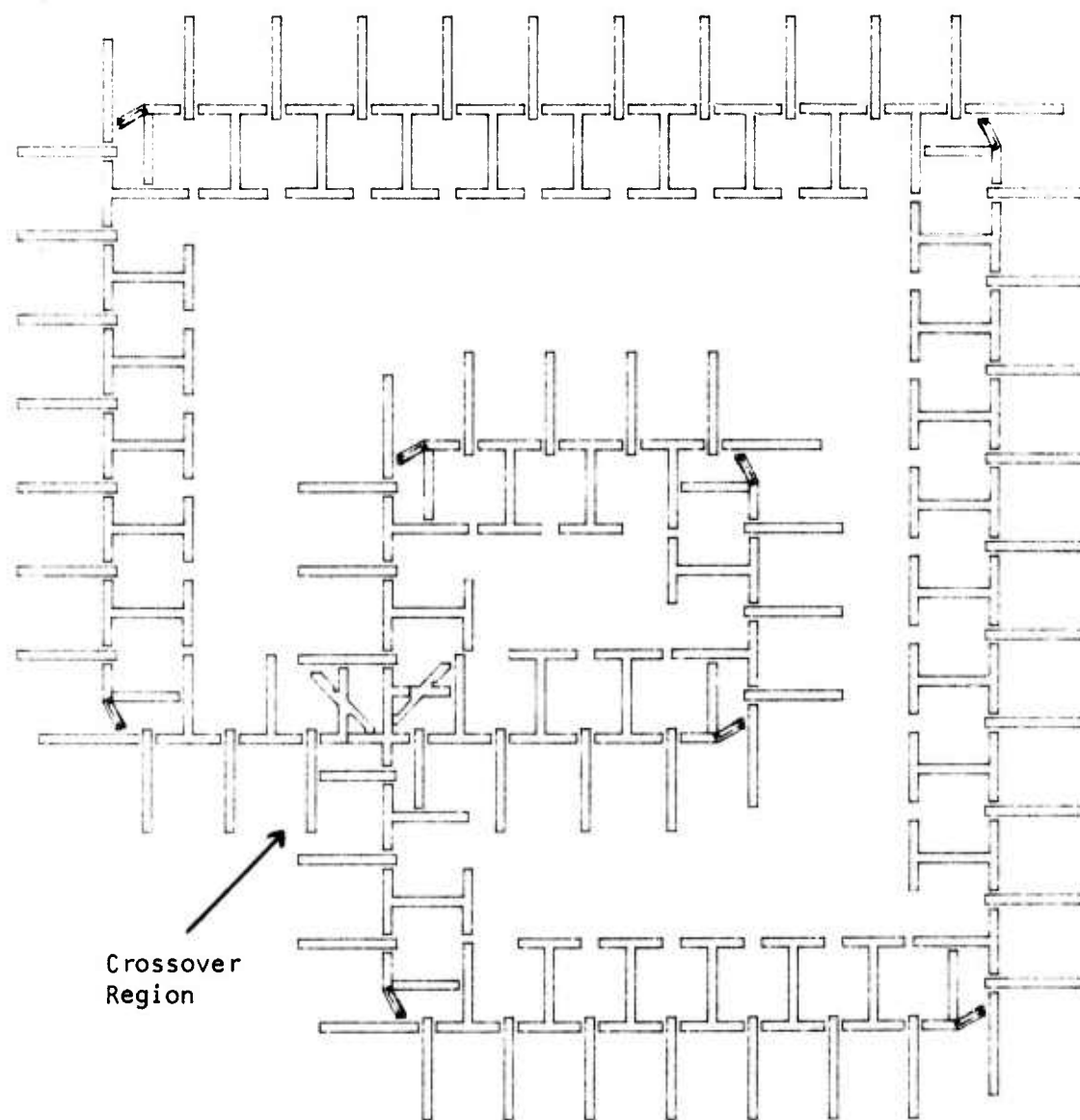


Figure 25 Permalloy Crossover Circuit

and gold conductor metallizations which are compatible with e-beam processing. The procedure involves plating through e-beam defined windows in PMMA photo-resist. Process improvement efforts are now concentrated on (1) improving the quality and reproducibility of the Permalloy and gold metallizations and (2) improving control on the e-beam pattern generator to obtain reproducibly narrow gaps between T's and bars.

In regard to improving the Permalloy, initial results indicated poor control on the deposition rate during the plating process from one run to the next. This lack of control has now been remedied.

Table V shows the results of plating five Permalloy film samples with different plating current densities, j , proportional to the deposition rates, and for different times, t . The rates and times were chosen to give films of constant thickness. The last column gives the thickness, T , and it is seen that T is constant to within about $\pm 9\%$ for the thicknesses shown. This degree of reproducibility was not obtained until the new process was implemented.

Table V
Permalloy Film Plating Results

<u>Sample</u>	<u>$j(\text{mA cm}^{-2})$</u>	<u>$t(\text{sec})$</u>	<u>$T(\text{\AA})$</u>
1	7.89	120	1438
2	9.86	96	1463
3	5.92	160	1375
4	11.83	80	1375
5	13.81	68	1225

Compositional control of the Permalloy depends on the parameters of the plating bath. We are in the process of establishing the conditions for the zero magnetostriction composition by measuring the strain sensitivity of films of different composition. The films are strained a known amount by bending, and the sensitivity to strain is measured by observing the magnetoresistive hysteresis loop in an applied ac magnetic field.⁹ The plating conditions for zero magnetostriction have now been identified, and further work will establish reproducibility. Our present films have coercivities comparable to vacuum deposited films (1 to 2 Oe), and so-called isotropic films are easily obtained.

Improvements in the stability of the e-beam pattern generator are being made to gain further control on pattern dimensions. Ripple on the voltages applied to the electron optics is being removed. It is expected that this change will make it possible to produce more regular patterns with uniformly narrow gaps between T's and bars. We expect to produce high quality patterns over at least a 30 mil x 30 mil field corresponding to about 10^5 bits. Some plated Permalloy circuits of this size have now been made on glass substrates, and no difficulties from nonuniform plating have been encountered.

Figures 26 through 29 are a series of optical and scanning electron micrographs illustrating the results of plating Permalloy on e-beam defined patterns in 3400 Å thick PMMA photoresist on glass substrates. Three thicknesses of Permalloy are illustrated. Nine fields of 1000 bit T-bar circuits were exposed and plated in each case. The circuit period is 2.4 μm. One mil wide fiducial marks are placed between the fields to aid in locating the patterns for observation in the SEM.

Optical photomicrographs illustrating these fields are shown in Figure 26 for magnifications of 62X, 126X, 495X, and 637X. This series demonstrates that submicrometer linewidth devices can be seen with conventional microscopes and indicates that optical access will be possible, although diffraction of light around the elements is bothersome to the observer.

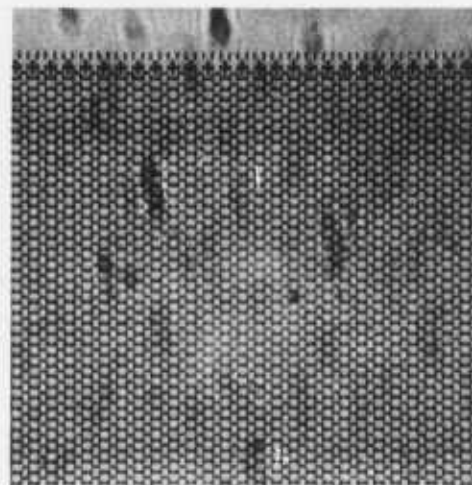
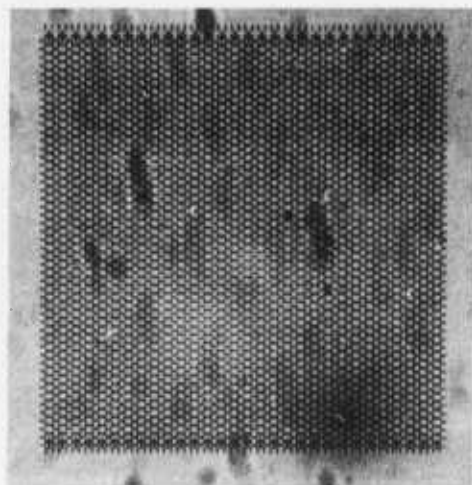
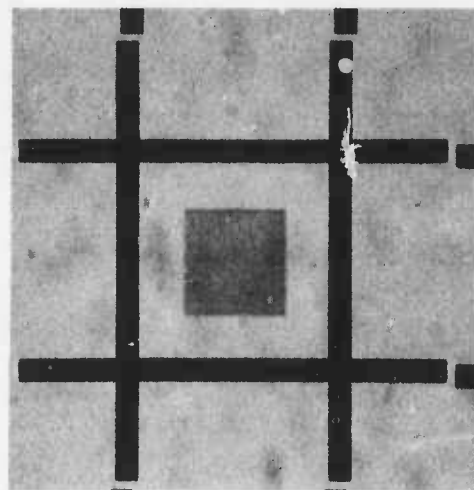
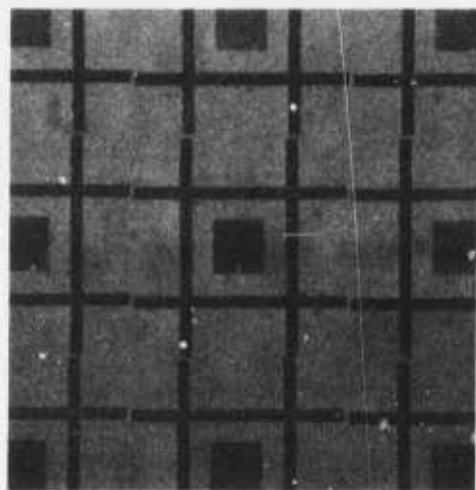


Figure 26 Optical Micrographs of E-Beam Patterned T-Bar Fields

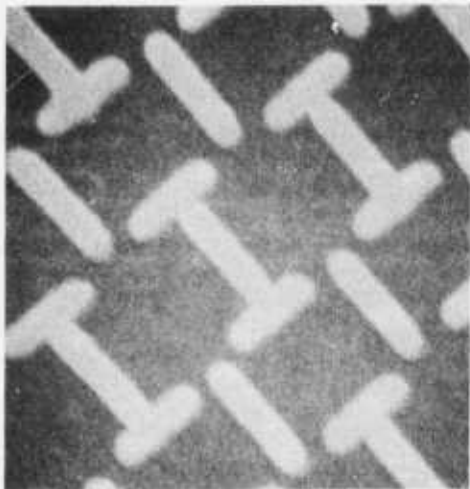
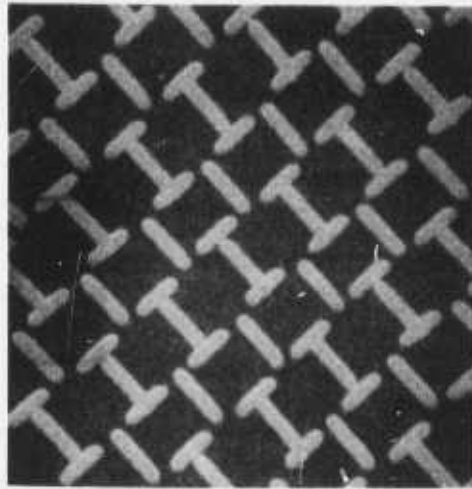
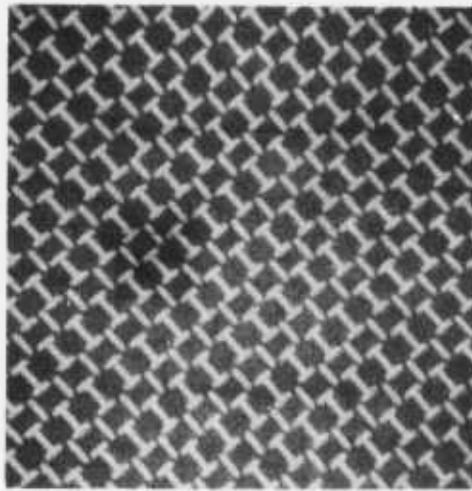


Figure 27 Scanning Electron Micrographs of 750 Å Thick Permalloy Elements

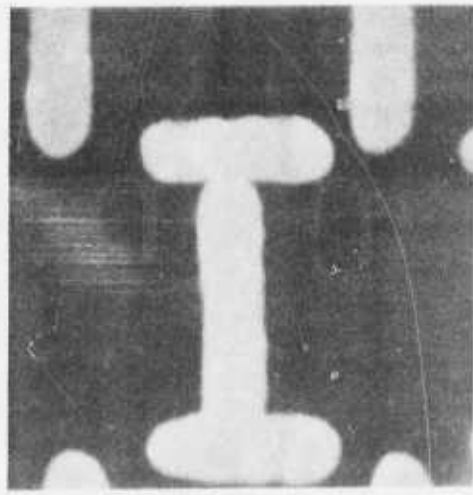
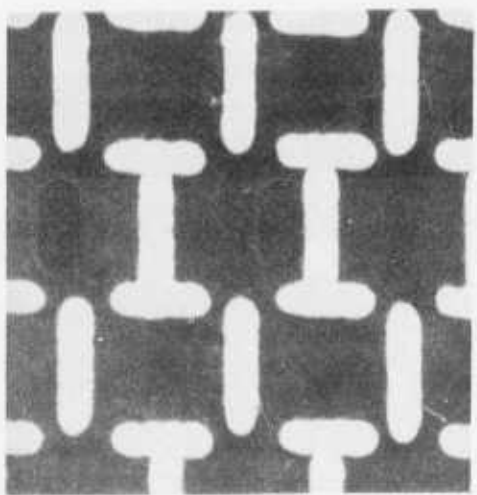
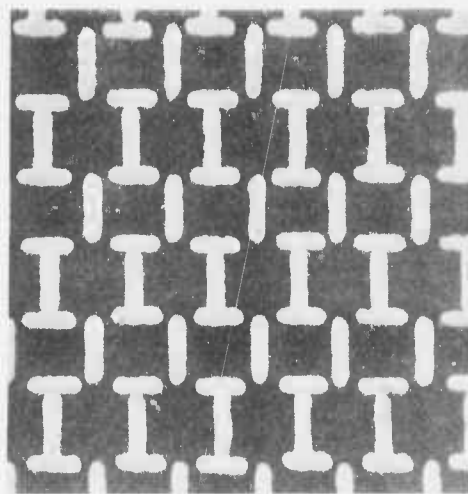
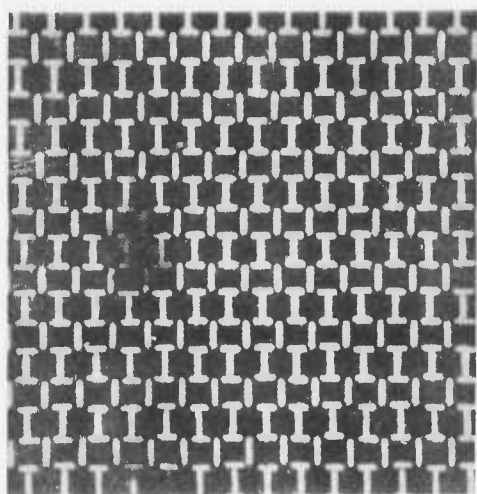


Figure 28 Scanning Electron Micrographs of 1700 Å Thick Permalloy Elements

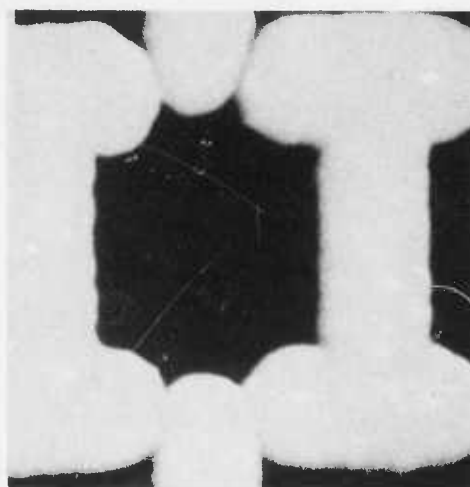
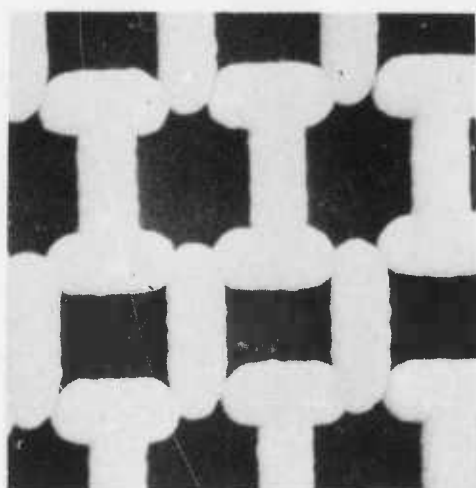
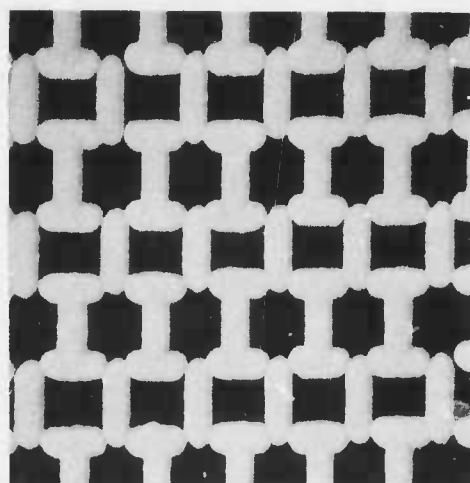
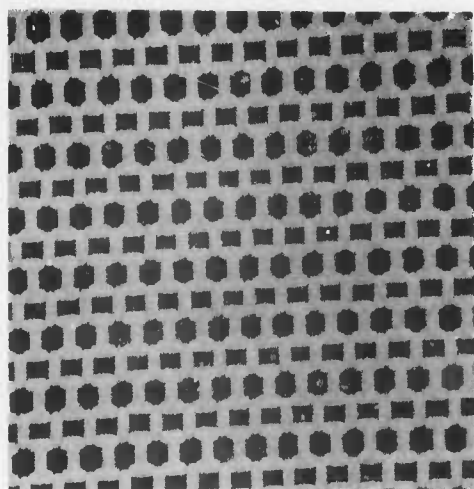


Figure 29 Scanning Electron Micrographs of 3800 Å Thick Permalloy Elements

The first series of SEM's, Figure 27, shows 750 Å thick Permalloy elements at magnifications of 2400X, 6000X, 12,000X, and 24,000X. Permalloy granularity is not apparent, and the gaps are well opened, but a little too wide for good bubble propagation. Also, the bars should be a little longer. A second example is shown in Figure 28 for elements 1700 Å thick. In a third example, Figure 29, we intentionally plated through the 3400 Å thick resist windows with about 3800 Å of Permalloy. Here, the gaps are almost closed, but Permalloy granularity is still not evident. The sample tilt angle was 13° for all the SEM's. From results such as these we conclude that plated Permalloy elements in excess of 1700 Å thick are practical for 2.4 μm circuit periods.

In order to have complete circuit processing capability, there must be a conductor metallization process that is compatible with the Permalloy process and the e-beam pattern process in PMMA photoresist. The conductor process must also give films having (1) low intrinsic stress to avoid trapping bubbles in the stress-field gradients, (2) small grain size to give good pattern definition, and (3) small grain size to inhibit electromigration at high current densities. To satisfy these requirements, we are investigating plated gold. The grain size in these films is comparable to that in Permalloy. With further work the plating process is expected to give the required conductor metallization properties.

2. Garnet Material for Small Bubbles

The garnet composition that we have chosen for the initial small bubble devices is $(\text{LuSm})_3\text{Fe}_5\text{O}_{12}$. For our particular composition $l \approx 0.06 \mu\text{m}$, and q (the ratio of the anisotropy field, H_k , to $4\pi M_s$, the magnetization) has been maximized under the constraint that the lattice constant of the epitaxial film, a_f , can be matched to that for the GGG substrate, a_0 . This conclusion follows from the data of Gyorgy,¹⁰ who showed that the growth anisotropy is greatest for the samarium ion

in a lutetium host garnet. By adding the larger samarium ion to its maximum concentration under the $a_f \simeq a_o$ constraint, we have maximized K_u , the growth anisotropy.

Additional growth anisotropy could be obtained by permitting the samarium content to increase, thus placing the epitaxial film into compression. It seems unnecessary at present to use this technique and risk film cracking or growth faceting; therefore, we will continue to work with lattice matched films. Other workers, however, are employing large compressional lattice mismatches for small-bubble material.¹¹

What has been sacrificed in the choice of composition? Since Lu^{+3} is a closed shell ion, its behavior is similar to Y^{+3} , a low damping ion. On the other hand, Sm^{+3} is an ion that is strongly coupled to the lattice and will cause the mobility, $\mu = \frac{\gamma^2}{\lambda} \left(\frac{A}{2\pi q} \right)^{1/2}$, to decrease.

$\gamma \equiv$ gyromagnetic ratio,

$\lambda \equiv$ the Landau-Lifshitz damping parameter, and

$A \equiv$ the exchange stiffness constant.

For the garnets the damping parameter, λ , divided by γ^2 is simply the averaged combination of the end members, i.e.,

$$\frac{\lambda}{\gamma^2} = \sum_i \frac{\lambda_i}{\gamma_i^2} g_i ,$$

where g_i is the fraction of the individual components in the unit garnet formula.

Since for our composition the samarium content per formula unit has been increased, one can expect the mobility to decrease somewhat. This decrease should not be detrimental for initial small-bubble devices.

Initial investigations of small-bubble propagation behavior have been performed by using the Vella-Coleira mobility circuit¹² processed directly on the garnet. Qualitative observations have been performed on $(\text{LuSm})_3\text{Fe}_5\text{O}_{12}$, but no accurate mobility data have been obtained due to the great difficulty in measuring submicrometer bubble diameters and the distance through which the bubbles travel. Most of the investigated material has not been ion implanted. The following conclusions were drawn from these observations.

- Bubble motion can be achieved with behavior similar to that observed for 5 μm diameter bubbles.
- The velocity is at least several hundred cm/sec for $\Delta H = 7$ Oersteds, the field difference across the bubble.
- A slight skewing angle ($< 20^\circ$) of the bubble away from the maximum field gradient is present.
- No hard bubbles were generated in the course of these observations.
- Motion is quite uniform for all the bubbles.

Concerning the observed skewing, it has not yet been determined how much skewing is allowable while achieving reliable propagation on Permalloy circuits. We believe that the skewing is small enough to permit us to begin initial device fabrication and testing.

Observations have also been made on ion-implanted $(\text{LuSm})_3\text{Fe}_5\text{O}_{12}$. One ion-implanted film ($5 \times 10^{14} \text{ cm}^{-2}$, 50 keV, neon) showed very erratic bubble

motion, with some bubbles hardly moving at all. Possibly, the implant was too deep for such a thin film. Further work is necessary to determine a satisfactory method for hard bubble suppression. Therefore, our first small bubble chips will probably be made from as-grown material.

Now that a set of e-beam compatible Permalloy processing steps and suitable garnet material are available, small-bubble device fabrication is ready to proceed. The first devices will consist of simple T-bar propagation circuits which will be studied with regard to bias field versus drive field margins. A particular objective in the initial phase of the device work is to investigate methods for reducing the high drive fields which have been recently reported^{13,14} for small-bubble devices.

C. Ion-Implant Field Access Circuits

An instrument for measuring garnet film magnetic susceptibility by the optical (Faraday rotation) technique was put into operation to measure K_u and K_1 , the uniaxial (growth) and cubic anisotropies, respectively.¹⁵ The magnetic field for the measurements is supplied by a 12-inch Varian magnet. The magnitude of K_1 is determined from the anisotropic behavior of susceptibility versus applied dc field for different orientations of the field in the plane of an epitaxial film. A fixture that allows the film/substrate composite to be strained along different in-plane directions allows the garnet magnetostriction constants, λ_{100} and λ_{111} , to be measured also.

This apparatus was used to determine the effectiveness of the steps we are taking to improve the ion-implant circuit garnets. The presence of an undesirable in-plane uniaxial component of anisotropy in garnets grown on poorly oriented substrates was confirmed. Previously, the anisotropy could only be inferred from device behavior. We also demonstrated that K_1 can be decreased by altering the

garnet composition. Moreover, materials from which devices having undesirable behavior were made have been shown to have large K_1 values. Again, the detrimental effects due to K_1 previously had only been inferred from the behavior of the devices. The detrimental effects resulting from K_1 and in-plane uniaxial anisotropy were described in AFAL-TR-74-19.

The in-plane anisotropy effect is illustrated in Figure 30. This sequence of micrographs shows an isolated bubble at different positions on the circumference of a 30 μm diameter disk on $(\text{YGdLu})_3(\text{FeGa})_5\text{O}_{12}$. This disk, which is covered by photoresist (hence its dark appearance), is surrounded by a region implanted with 150 eV, H_2^+ ions to a dose level of $3 \times 10^{16} \text{ cm}^{-2}$. At each bubble position the in-plane quasistatically rotating field is oriented along the direction of the radius vector defined by the center of the disk and the bubble. As the field rotates, bubble strip-out occurs over a fairly narrow range in angular position and reaches a maximum strip length. As stated previously, identification of this effect with misoriented substrates was confirmed by susceptibility measurements as a function of angular orientation in the plane of the film. Steps have been taken to provide more reproducibly precise substrate orientation after sawing and polishing. Additional data are required to assess the effectiveness of this procedure for improving operating devices.

For Figure 30 the in-plane rotating field was 28 Oe and the bias field was 104 Oe.

Our speculations concerning the effects of K_1 on the behavior of ion-implant devices were mentioned. To study these effects in more detail, garnet material was again patterned with isolated unimplanted disks. Observations of $(\text{YGdLu})_3(\text{FeGa})_5\text{O}_{12}$ implanted with this pattern showed the characteristic threefold symmetric tendency for bubbles to be trapped that we reported previously. This

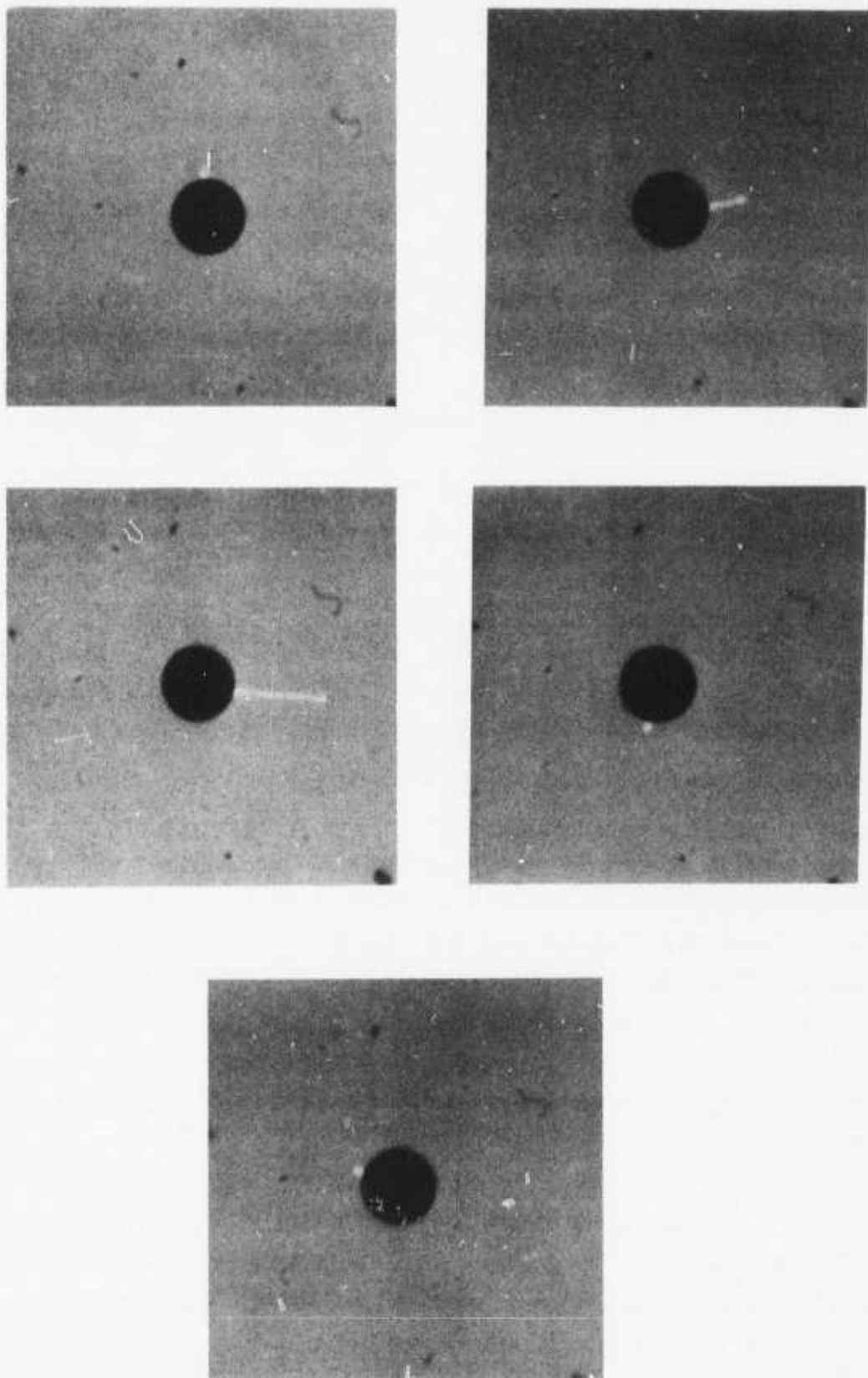


Figure 30 Effect of an In-Plane Uniaxial Component of Anisotropy

symmetry is tentatively ascribed to the in-plane effects of K_1 . If this conjecture is correct, the material composition is not yet optimized. To relate this behavior more closely to K_1 , we again employed the susceptibility apparatus to provide data from which in-plane anisotropy information could be derived. Efforts are under way to lower K_1 in $(\text{YGdLu})_3(\text{FeGa})_{5012}$ by the addition of certain minor constituents to the garnet composition. The results at this point are encouraging.

Some degradation with time is still being observed in ion-implant devices; i.e., newly fabricated devices work better than older devices. This degradation appears to be associated with the cusp regions on the propagation tracks defined by the ion-implant. Since it is known that some reduction of the garnet due to oxygen loss occurs during ion implantation, newly fabricated devices will be annealed in oxygen to restore stoichiometry. The aging process may be associated with large concentration gradients between the implanted and unimplanted regions.

Annealing furnaces for stabilizing ion-implant circuits against long-term degradation were set up and are now operating.

With these material improvements now available, we will resume regular fabrication of ion-implant circuits for continued study and evaluation.

A system for 1 MHz bubble propagation was breadboarded. The system can be operated in a startup/shutdown mode, with the current waveforms supplied to the drive coils remaining satisfactory during the transient periods. This system will find general use, but it will be particularly important for investigating the potential of ion-implant circuits as well as submicrometer bubble Permalloy circuits. The system consists of a pair of ENI power amplifiers having a bandwidth of 10 kHz to 10 MHz driving a pair of orthogonal field coils in series

resonant circuits. Shutdown is accomplished by discharging the tuning capacitors on the appropriate clock phase. Breadboard testing is complete, except for minor modifications to improve performance.

REFERENCES

1. L. Caron, "Variable Function Magnetic Domain Arrangement," U. S. Patent 3,750,106, 31 July 1973.
2. R. M. Smith, "Magnetic Domain Switching Matrix and Control Arrangement," U. S. Patent 3,753,253, 14 August 1973.
3. L. Caron, U. S. Patent 3,750,105, 31 July 1973.
4. M. Born and E. Wolf, Principles of Optics (Pergamon Press, New York, 1970,) p. 40.
5. P. K. Tien, R. Ulrich, and R. J. Martin, Appl. Phys. Letters 14, 291 (1969).
6. P. K. Tien and R. Ulrich, J. Opt. Soc. Am. 60, 1325 (1970).
7. S. Namba, H. Aritome, T. Nishimura, K. Masuda, and K. Toyoda, J. Vac. Sci. Technol. 10, 936 (1973).
8. P. I. Bonyhard, Y. S. Chen, and J. L. Smith, IEEE Trans. MAG-9, 708 (1973).
9. T. C. Penn and F. G. West, Rev. Sci. Instr. 35, 919 (1964).
10. E. M. Gyorgy, M. D. Sturge, L. G. Van Uitert, E. J. Heilner, and W. H. Grodkiewicz, J. Appl. Phys. 44, 438 (1973).
11. E. A. Giess, C. F. Guerici, J. D. Kuptsis, and H. L. Hu, Mat. Res. Bull. 8, 1061 (1973).
12. G. P. Vella-Coleiro and W. J. Tabor, Appl. Phys. Letters 21, 7 (1972).
13. M. H. Kryder, K. Y. Ahn, G. S. Almasi, G. E. Keefe, and J. V. Powers, Paper 26-2, Intermag Conference, Toronto, Canada, 14-17 May 1974.
14. P. K. George, J. Hughes, and J. L. Archer, Paper 26-1, Intermag Conference, Toronto, Canada, 14-17 May 1974.
15. P. W. Shumate, Jr., D. H. Smith, and F. B. Hagedorn, J. Appl. Phys. 44, 449 (1973).